




























Detailed Asteroseismic Modeling of the High-luminosity Red-giant Branch Host Stars KOI-3886 and ι Draconis

TIAGO L. CAMPANTE ^{1,2} TANDA LI ^{3,4} J. M. JOEL ONG ⁵ ENRICO CORSARO ⁶ MARGARIDA S. CUNHA ^{1,2}
TIMOTHY R. BEDDING ^{7,4} DIEGO BOSSINI ¹ TIMOTHY D. BRANDT ⁸ SYLVAIN N. BRETON ⁹
DEREK L. BUZASI ¹⁰ WILLIAM J. CHAPLIN ^{3,4} MORGAN DEAL ¹ RAFAEL A. GARCÍA ⁹ MICHELLE L. HILL ¹¹
MARC HON ^{12,13} DANIEL HUBER ¹² CHEN JIANG ^{14,15} STEPHEN R. KANE ¹¹ CENK KAYHAN ¹⁶
JAMES S. KUSZLEWICZ ^{14,4} JORGE LILLO-BOX ¹⁷ SAVITA MATHUR ^{18,19} MÁRIO J. P. F. G. MONTEIRO ^{1,2}
FILIPE PEREIRA ^{1,2} NUNO C. SANTOS ^{1,2} ALDO SERENELLI ^{20,21} AND DENNIS STELLO ^{13,4}

¹*Instituto de Astrofísica e Ciências do Espaço, Universidade do Porto, Rua das Estrelas, 4150-762 Porto, Portugal*

²*Departamento de Física e Astronomia, Faculdade de Ciências da Universidade do Porto, Rua do Campo Alegre, s/n, 4169-007 Porto, Portugal*

³*School of Physics and Astronomy, University of Birmingham, Edgbaston, Birmingham B15 2TT, UK*

⁴*Stellar Astrophysics Centre (SAC), Department of Physics and Astronomy, Aarhus University, Ny Munkegade 120, 8000 Aarhus C, Denmark*

⁵*Department of Astronomy, Yale University, 52 Hillhouse Ave., New Haven, CT 06511, USA*

⁶*INAF — Osservatorio Astrofisico di Catania, via S. Sofia 78, 95123 Catania, Italy*

⁷*Sydney Institute for Astronomy (SIfA), School of Physics, University of Sydney, NSW 2006, Australia*

⁸*Department of Physics, University of California, Santa Barbara, Santa Barbara, CA 93106, USA*

⁹*AIM, CEA, CNRS, Université Paris-Saclay, Université Paris Diderot, Sorbonne Paris Cité, F-91191 Gif-sur-Yvette, France*

¹⁰*Department of Chemistry and Physics, Florida Gulf Coast University, 10501 FGCU Blvd. S., Fort Myers, FL 33965, USA*

¹¹*Department of Earth and Planetary Sciences, University of California Riverside, 900 University Ave., Riverside, CA 92521, USA*

¹²*Institute for Astronomy, University of Hawai'i, 2680 Woodlawn Drive, Honolulu, HI 96822, USA*

¹³*School of Physics, The University of New South Wales, Sydney NSW 2052, Australia*

¹⁴*Max-Planck-Institut für Sonnensystemforschung, Justus-von-Liebig-Weg 3, 37077 Göttingen, Germany*

¹⁵*School of Physics and Astronomy, Sun Yat-Sen University, No. 135, Xingang Xi Road, Guangzhou 510275, P. R. China*

¹⁶*Department of Astronomy and Space Sciences, Erciyes University, 38030, Kayseri, Turkey*

¹⁷*Centro de Astrobiología (CAB, CSIC-INTA), Depto. de Astrofísica, ESAC Campus 28692 Villanueva de la Cañada (Madrid), Spain*

¹⁸*Instituto de Astrofísica de Canarias (IAC), E-38205 La Laguna, Tenerife, Spain*

¹⁹*Universidad de La Laguna (ULL), Departamento de Astrofísica, E-38206 La Laguna, Tenerife, Spain*

²⁰*Institute of Space Sciences (ICE, CSIC) Campus UAB, Carrer de Can Magrans, s/n, E-08193, Bellaterra, Spain*

²¹*Institut d'Estudis Espacials de Catalunya (IEEC), Carrer del Gran Capità, 2-4, E-08034, Barcelona, Spain*

ABSTRACT

Asteroseismology is playing an increasingly important role in the characterization of evolved host stars and their planetary systems. Here, we present the detailed asteroseismic modeling of two high-luminosity red-giant branch (HLRGB) hosts, KOI-3886 and ι Draconis, having made use of end-of-mission *Kepler* (KOI-3886) and multi-sector TESS (ι Draconis) time-series photometry. This completes a series of three articles dedicated to these systems by providing a full account of the underlying seismic analyses. We first test the impact of adopting different sets of observed modes as seismic constraints. Inclusion of $\ell = 1$ and 2 modes improves the precision, albeit marginally, on the stellar properties compared to radial modes alone, with 1.8–3.0% (radius), 5–9% (mass), and 19–25% (age) reached when using pure π modes as constraints. Given the small period spacing of dipole mixed modes, the sparse set of observed g-dominated modes is not able to provide extra constraints, resulting in highly multimodal posteriors. Consequently, detailed modeling of HLRGB stars based on (lower-resolution) TESS power spectra attains a precision commensurate with that based on end-of-mission *Kepler* data. Furthermore, we test the impact of varying the atmospheric boundary condition. We

find mass and radius estimates to be insensitive to the description of the near-surface layers, at the expense of substantially changing both the near-surface structure of the best-fitting models and the values of associated parameters like the initial helium abundance, Y_i . Attempts to measure Y_i from seismic modeling of red giants may thus be systematically dependent on the choice of atmospheric boundary condition.

Keywords: asteroseismology — stars: evolution — stars: fundamental parameters — stars: individual (HD 190655, HD 137759, TYC 3130-2385-1)

1. INTRODUCTION

Throughout the course of the NASA *Kepler*/K2 mission (Borucki et al. 2010; Howell et al. 2014), asteroseismology has played an important role in the characterization of host stars and their planetary systems (for recent reviews, see Campante et al. 2018; Lundkvist et al. 2018). *Kepler*/K2 mainly targeted main-sequence stars, however, observing too few red giants to detect enough planets for robust statistics (Grunblatt et al. 2017, 2019). This meant that the synergy between asteroseismology and exoplanetary science would remain mostly confined to unevolved stars. The advent of NASA’s *Transiting Exoplanet Survey Satellite* (TESS; Ricker et al. 2015) has since lifted this restriction, as it enables the systematic search for transiting planets around seismic giants (Campante et al. 2016; Huber et al. 2019; Pereira et al. 2019; Grunblatt et al. 2022; Saunders et al. 2022), as well as revisiting previously known (mostly from radial-velocity surveys) evolved hosts using asteroseismology (Campante et al. 2019; Ball et al. 2020; Jiang et al. 2020; Nielsen et al. 2020; Kane et al. 2021).

The high-luminosity red-giant branch (HLRGB) host stars KOI-3886 A (HD 190655, KIC 8848288, TIC 185060864; hereafter KOI-3886) and ι Draconis (HD 137759, TIC 165722603; hereafter ι Dra) are paradigmatic cases in this regard (see Table 1 for a compilation of their properties as found in the literature and Fig. 1 for their location on an HR diagram). KOI-3886, observed by *Kepler* for nearly 4 years and later by TESS over 1 sector (27.4 days), has been a longtime candidate host (Rowe et al. 2015). In Lillo-Box et al. (2021), we concluded that the close-in planet candidate is in fact a false positive and reinterpreted the system as an eclipsing brown dwarf in a hierarchical triple containing two evolved stars. The fundamental stellar properties derived from asteroseismology for KOI-3886 (the primary) were central to that work, eventually entering an iterative procedure to determine a final set of properties for the three bodies in the system.

ι Dra, known for two decades to host a planet¹ in a highly eccentric, 511-day-period orbit (Frink et al. 2002; Zechmeister et al. 2008; Kane et al. 2010), was observed by TESS over 5 sectors. In Hill et al. (2021), we presented the results of continued radial-velocity (RV) monitoring of ι Dra over several orbits of its known planet. The newly acquired RV observations allowed us to detect curvature in the previously identified RV trend, which was interpreted as likely being caused by an outer companion. Making use of the precise seismic mass derived for ι Dra, we were able to improve on the precision of planet b’s minimum mass. Moreover, through combination of the RV measurements with space astrometry, we confirmed the presence of an additional long-period, eccentric companion. Mass predictions from our analysis — which used the seismic stellar mass as a prior — place the companion on the border of the planet and brown dwarf regimes.

The presence of planets orbiting KOI-3886 and ι Dra (putative in the former case) is what originally motivated the detailed seismic analyses — conducted separately, although not in a strictly independent manner — of these two K giants. With the present follow-up paper, we complete a *trilogy* dedicated to these systems by providing a full account of the seismic analyses underpinning Lillo-Box et al. (2021) and Hill et al. (2021), placing special emphasis on the detailed asteroseismic modeling of both stars.

Forward modeling of individual mode frequencies (other than radial modes) of HLRGB stars is a state-of-the-art affair (Li et al. 2018; Ong et al. 2021a). Evolutionary calculations in this phase of evolution are particularly sensitive to small variations in the choices of input physics and model parameters, in a highly nonlinear fashion. For instance, small variations in the amount of envelope overshooting result in shifts to both the age and luminosity at which the red-giant luminosity bump occurs, as well as lateral adjustments to the position

¹ ι Dra b was the first planet found to orbit a giant star (Frink et al. 2002).

130 of the red-giant branch itself on the HR diagram (e.g.,
 131 Khan et al. 2018). These changes are degenerate with
 132 those induced by variations in the mixing-length param-
 133 eter, α_{MLT} , and the initial helium abundance, Y_i , neither
 134 of which can be directly constrained in cool stars. The
 135 same is also true of other inputs to stellar evolution, such
 136 as the reference values used for solar composition (e.g.,
 137 Grevesse & Sauval 1998; Asplund et al. 2009), equa-
 138 tions of state, or opacity tables, which are not typically
 139 treated as variable parameters in grids of stellar models
 140 used for this purpose.

141 To make matters worse, the observational phe-
 142 nomenology for these evolved oscillators requires the in-
 143 volvement of both the usual acoustic waves in the con-
 144 vective stellar exterior, as well as buoyancy waves con-
 145 fined to the stellar interior, in order to fully describe
 146 the observed normal modes, which possess mixed p-
 147 (or pressure) and g-mode (or gravity) character (e.g.,
 148 Aizenman et al. 1977; Unno et al. 1989). The treat-
 149 ment of these mixed modes is a numerically sensitive
 150 affair (Christensen-Dalsgaard et al. 2020), and the use
 151 of mixed modes in stellar modeling itself involves both
 152 great computational expense (Ong et al. 2021b) and
 153 theoretical sophistication. While modes of quadrupole
 154 or higher degree in these red giants may be treated as
 155 purely acoustic waves to a good approximation (e.g.,
 156 Ball et al. 2018), the use of such a prescription for the
 157 dipole modes, which are an order of magnitude more
 158 strongly mixed (Ong et al. 2021a), is largely untested.

159 Herein, we test the impact of the optimization pro-
 160 cedure by conducting detailed asteroseismic modeling
 161 based on three alternative approaches, namely, by using
 162 the full mode frequency lists (which include g-dominated
 163 modes), pure π modes alone (i.e., adopting the most p-
 164 dominated mixed modes), and only considering radial
 165 modes. Furthermore, we test the impact of varying the
 166 input physics, namely, the treatment of the model at-
 167 mosphere, on the inferred fundamental stellar proper-
 168 ties. This work hence constitutes a valuable incursion
 169 into the problematic of detailed asteroseismic model-
 170 ing of HLRGB stars, for which we make use of high-
 171 quality, end-of-mission *Kepler* (KOI-3886) and multi-
 172 sector TESS (ι Dra) time-series photometry.

173 The rest of this paper is organized as follows. In
 174 Sect. 2, we present the adopted *Kepler* and TESS pho-
 175 tometry. This is followed in Sect. 3 by the analysis of
 176 both data sets, including the measurement of individ-
 177 ual mode frequencies. Detailed asteroseismic modeling
 178 is performed in Sect. 4. Finally, a summary and conclu-
 179 sions are presented in Sect. 5.

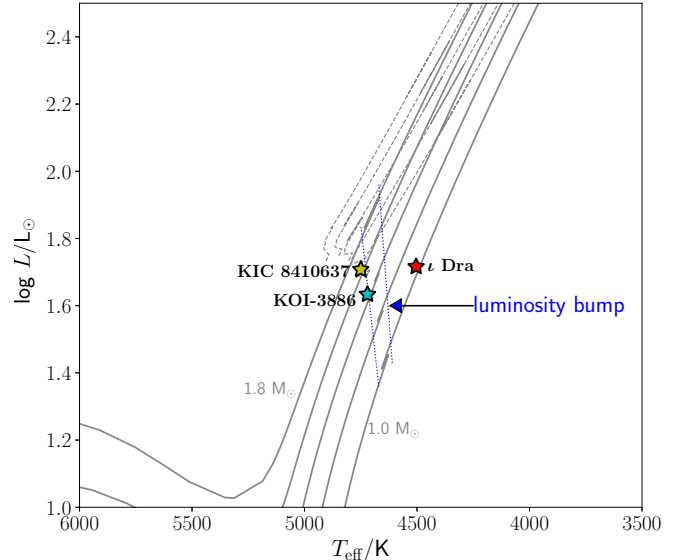


Figure 1. Location of KOI-3886 and ι Dra on an HR diagram. The benchmark star KIC 8410637 (see Sect. 4) is also displayed. Stellar evolutionary tracks ranging in mass from 1.0 to 1.8 M_{\odot} (in steps of 0.2 M_{\odot}) are shown as solid curves while on the red-giant branch. The location of the red-giant luminosity bump across tracks is delimited by the dotted lines.

181 KOI-3886 was observed by *Kepler* in long-cadence
 182 mode (29.4 minutes) between Quarters 0 and 17 (or
 183 for nearly 4 years). It would also be later observed
 184 by TESS during Sector 14 (27.4 days) at a faster 2-
 185 minute cadence. Owing to the much shorter temporal
 186 coverage of TESS observations, we have nonetheless de-
 187 cided to base the seismic analysis of KOI-3886 solely
 188 on the available *Kepler* photometry. We make use of a
 189 KEPSEISMIC² light curve, which has been optimized for
 190 asteroseismology. The light curve was extracted from
 191 the target pixel files using a custom aperture and sub-
 192 sequently processed through the KADACS pipeline (*Ke-*
 193 *pler* Asteroseismic Data Analysis and Calibration Soft-
 194 ware; García et al. 2011). KADACS corrects for outliers,
 195 jumps, and drifts, also filling any gaps shorter than 20
 196 days using in-painting techniques (García et al. 2014;
 197 Pires et al. 2015). The light curve was further high-pass
 198 filtered using an 80-day triangular smoothing function,
 199 after which it underwent an iterative (three iterations)
 200 σ -clipping procedure (3σ level) in order to mitigate the
 201 impact of the eclipses on the computation of the power
 202 spectrum. Figure 2 (left panel) shows Quarter 9 of the
 203 resulting *Kepler* light curve.

² <https://archive.stsci.edu/prepds/kepseismic/>

2. PHOTOMETRY

Table 1. Stellar properties for KOI-3886, ι Dra, and KIC 8410637.

	KOI-3886		ι Dra		KIC 8410637 ^a	
Parameter	Value	Source	Value	Source	Value	Source
<i>Gaia</i> Photometry and Parallax						
EDR3 ID	2082133182277361152	1	1614731957531452544	1	2105415749007167616	1
<i>G</i> -band Mag.	10.1	1	2.97	1	10.8	1
π (mas)	2.139±0.307	1	32.52±0.14	1	0.839±0.018	1
Spectroscopy						
T_{eff} (K)	4720±120	2	4504±62	3,4	4750±86	5
[Fe/H] (dex)	0.14±0.07	2	0.03±0.08	3,4	0.12±0.08	5
log g (cgs)	2.54±0.24	2	2.52±0.07	3,4	2.75±0.15	5
Spectral Energy Distribution (SED) / Joint Light and Velocity Curve Analysis						
L (L_{\odot})	43.3±9.5	2	52.8±2.1	4	51.2 ^{+4.0} _{-3.7}	6
<i>Reference</i> Fundamental Stellar Properties						
M (M_{\odot})	1.56±0.03 ^c	6
R (R_{\odot})	11.99±0.06 ^b	7	10.74±0.11 ^c	6
Global Asteroseismology						
$\Delta\nu$ (μHz)	4.60 ± 0.20	8	4.02 ± 0.02	8	4.63±0.01	5
ν_{max} (μHz)	46.9 ± 0.3	8	38.4 ± 0.5	8	46.3±0.9	5

^aBenchmark star (see Sect. 4).

^bFrom interferometry.

^cFrom the dynamical modeling of the eclipsing binary’s orbit.

References—(1) Gaia Collaboration et al. (2021), (2) Lillo-Box et al. (2021), (3) Jofré et al. (2015), (4) Hill et al. (2021), (5) Li et al. (2018), (6) Frandsen et al. (2013), (7) Baines et al. (2011), (8) this work.

204 ι Dra was observed by TESS during Sectors 15–16 and
 205 22–24 at a 2-minute cadence. The target’s high bright-
 206 ness (apparent TESS magnitude of $T = 2.27$) leads to
 207 saturation of the central pixels of a stellar image dur-
 208 ing a 2-second exposure (each TESS camera acquires a
 209 new image every 2 s). To deal with the target’s satu-
 210 rated nature, a large custom aperture was adopted and
 211 a background model applied to account for the spatially-
 212 varying background light (full details on the light curve
 213 preparation are given in Hill et al. 2021). There is no
 214 detection of a transit signal in the full TESS light curve.
 215 Figure 2 (right panel) shows Sectors 22–24 of the result-
 216 ing TESS light curve.

217 3. ASTEROSEISMOLOGY

218 3.1. Global Oscillation Parameters

219 Figure 3 shows the power density spectra of KOI-3886
 220 (left panel) and ι Dra (right panel) based on the Lomb–

221 Scargle periodogram (Lomb 1976; Scargle 1982) of the
 222 light curves extracted in Sect. 2. These reveal a clear
 223 power excess due to solar-like oscillations at $\sim 50 \mu\text{Hz}$
 224 and $\sim 40 \mu\text{Hz}$, respectively. We measured the large
 225 frequency separation, $\Delta\nu$, and the frequency of max-
 226 imum oscillation amplitude, ν_{max} , of both stars using
 227 a range of well-tested automated methods (e.g., Huber
 228 et al. 2009; Mathur et al. 2010; Corsaro & De Ridder
 229 2014; Campante et al. 2017, 2019; Corsaro et al. 2020).
 230 Consolidated pairs of values are listed in Table 1 and
 231 stem from a single method for each star (for details, see
 232 Lillo-Box et al. 2021; Hill et al. 2021), their uncertainties
 233 being the corresponding formal uncertainties.

234 3.2. Individual Mode Frequencies

235 We extracted individual mode frequencies from the
 236 power spectrum of each star (a process dubbed *peak-*
 237 *bagging*) using the FAMED pipeline (Fast and AutoMated

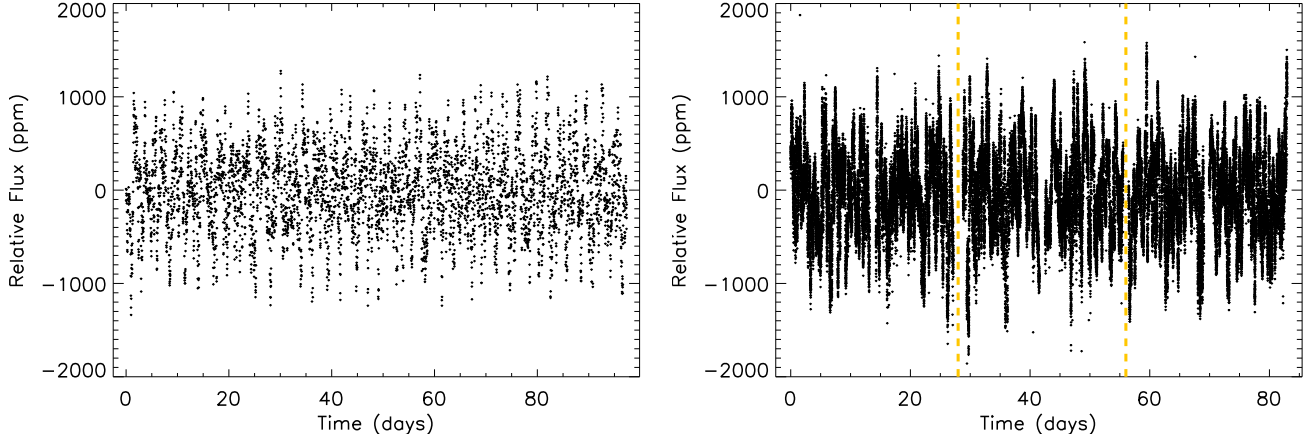


Figure 2. *Left Panel:* Segment of the *Kepler* light curve of KOI-3886 (Quarter 9). The light curve has been resampled onto a regular grid and short gaps filled. *Right Panel:* Segment of the TESS light curve of ι Dra (Sectors 22–24). Vertical dashed lines mark the transition between sectors. Intra-sector gaps are due to the data downlink, separating the two spacecraft orbits in each sector. Note the higher cadence and thus larger density of data points with respect to the *Kepler* light curve.

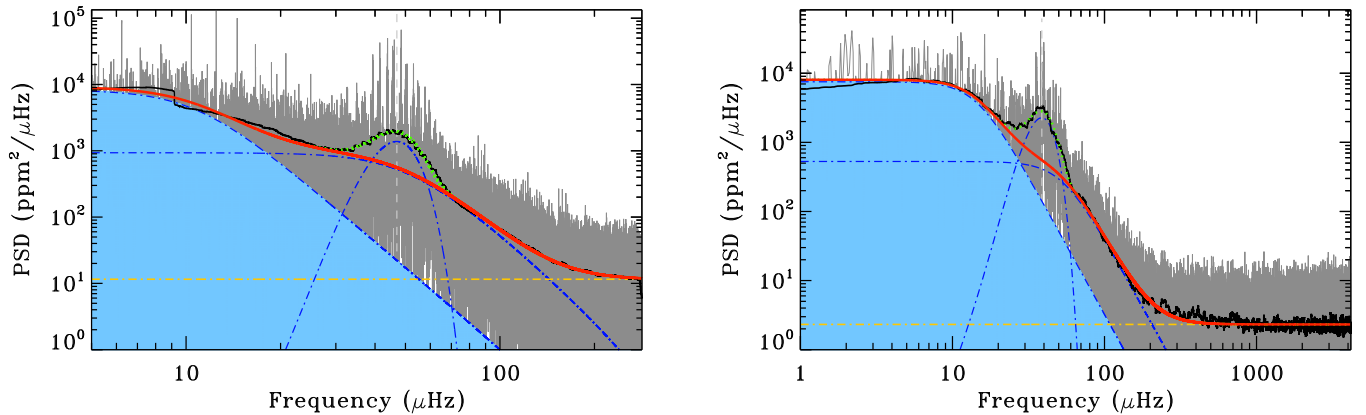


Figure 3. Power spectral density (PSD) of KOI-3886 (left panel) and ι Dra (right panel). Power spectra are shown in gray (heavily smoothed version in black). Vertical dashed lines are proxies for ν_{\max} . Solid red curves are fits to the background performed with DIAMONDS (Corsaro & De Ridder 2014), consisting of two Harvey-like profiles (blue dot-dashed curves) and a white noise offset (yellow dot-dashed line). Joint fits to the oscillation power excess (blue dot-dashed Gaussian) and background are visible as green dotted curves near ν_{\max} . Note the smaller frequency range of the PSD of KOI-3886, owing to the lower Nyquist frequency of *Kepler*'s long-cadence data. A residual signature of the eclipse harmonics can still be seen at the low-frequency end in the PSD of KOI-3886.

238 peak bagging with DIAMONDS; Corsaro et al. 2020). Ta-
 239 bles A1 and A2 list all significant^{3,4} modes returned by
 240 FAMED for KOI-3886 and ι Dra, respectively. A total

³ A peak is tested against the noise only if its height in the smoothed power spectrum is lower than 10 times the local background level, otherwise it is automatically considered as detected (denoted as ‘—’ in Tables A1 and A2). A detection probability (p_{det}) is computed for each low- S/N peak based on a Bayesian model comparison, peaks being deemed significant if $p_{\text{det}} \geq 0.993$. See sect. 5.3 of Corsaro et al. (2020) for details.

⁴ The Doppler shift of the observed mode frequencies due to the line-of-sight motion (Davies et al. 2014) is not significant for either star and hence no correction has been applied.

241 of 34 (23) modes of angular degree $\ell = 0, 1, 2$, and 3
 242 were extracted across 8 (7) radial orders for KOI-3886
 243 (ι Dra). Figures A1 and A2 illustrate the outcome of
 244 the peak-bagging process.

245 Owing to the lower resolution of the TESS power spec-
 246 trum of ι Dra, we have introduced an additional step
 247 for selecting mode frequency lists for this star, which
 248 combines the output of several peak-bagging procedures.
 249 This was mainly motivated by the need to robustly iden-
 250 tify and measure long-lived mixed modes. Several *peak-*
 251 *baggers* ($N = 7$) initially extracted individual mode
 252 frequencies from the power spectrum of ι Dra. The
 253 methods employed included both iterative sine-wave fit-

ting (e.g., Lenz & Breger 2005) as well as the fitting of Lorentzian and sinc² mode profiles (e.g., Handberg & Campante 2011), the latter approach being the one implemented in FAMED. Two frequency lists were then produced following the procedure described in Campante et al. (2011), namely, a *maximal frequency list* and a *minimal frequency list*. The former includes modes detected by at least 2 peak-baggers, whereas the latter includes only those modes detected by more than $\lfloor N/2 \rfloor$ peak-baggers. The more conservative minimal list is thus a subset of the maximal list. Importantly, modes in the minimal list are the ones subject to detailed modeling in Sect. 4. To guarantee reproducibility, we resort to a set of observed mode frequencies (and corresponding uncertainties) tracing back to a single method (FAMED), as opposed to an averaged set. We note that Zechmeister et al. (2008), using RV measurements, detected the presence of solar-like oscillations in ι Dra with frequencies around $3\text{--}4\text{ d}^{-1}$ ($\sim 35\text{--}46\ \mu\text{Hz}$), fully consistent with our results. The dominant mode (3.45 d^{-1}) found by those authors coincides with one of the radial modes in the minimal list.

3.3. Evolutionary State

Prior knowledge of the evolutionary state of either star is crucial towards an accurate determination of their fundamental properties in Sect. 4. KOI-3886 has been classified in the literature as a hydrogen-shell burning red giant (or RGB) following a number of complementary analyses of its oscillation power spectrum, namely, based on the pressure-mode pattern (Kallinger et al. 2012; Vrad et al. 2018), the morphology of the mixed modes (Elsworth et al. 2017), and deep learning (Hon et al. 2017). The evolutionary state of ι Dra, on the other hand, remains (seismically) unclassified, and we have adopted a number of approaches in this work to address this.

Given the limited number of observed dipole mixed modes per radial order, estimation of the observed period spacing (ΔP ; Bedding et al. 2011) of ι Dra based on modes in the minimal list proved unsuccessful. An attempt was then made at constraining the asymptotic period spacing, $\Delta\Pi_1$, based on the stretching of the power spectrum (Vrad et al. 2016), which again was inconclusive. Alternatively, the asymptotic acoustic-mode offset, ε_c , can in principle be used as a discriminant between hydrogen-shell burning (RGB) and helium-core burning (HeB) red giants (Kallinger et al. 2012; Christensen-Dalsgaard et al. 2014). The measured value of $\varepsilon_c = 0.95 \pm 0.11$, however, lies very close (within 1σ) to the decision boundary of Kallinger et al. (2012),

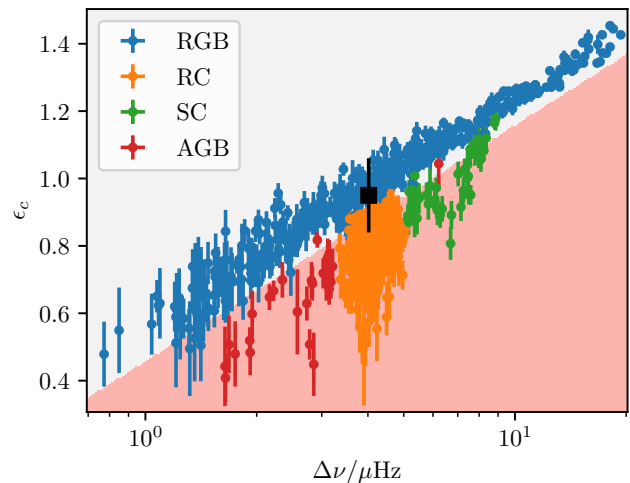


Figure 4. Classification of ι Dra using the p-mode phase offset, ε_c . We show the data set from fig. 4 of Kallinger et al. (2012) as colored points (‘RGB’ = red-giant branch, ‘RC’ = red clump, ‘SC’ = secondary clump, ‘AGB’ = asymptotic-giant branch) and the measured value of ε_c for ι Dra as the black square. In the background, we show, using shaded regions, the decision boundary of a one-vs-rest support vector machine classifier fitted against the first-ascent red giants of Kallinger et al. (2012). ι Dra lies close enough to the decision boundary that either a first-ascent red giant or red-clump star are plausible descriptions of it.

potentially allowing for either evolutionary state with this rudimentary method (see Fig. 4).

Machine learning classification methods provided the first robust indication that ι Dra is an RGB star. We ran the time-domain classifier CLUMPINESS (Kuszlewicz et al. 2020) over the full TESS light curve, as well as the two contiguous data subsets, i.e., Sectors 15–16 and Sectors 22–24. The probability of the star being on the RGB is respectively $p = 0.78$, 0.56 , and 0.81 . The corresponding probability of it being an HeB star is $p = 0.21$, 0.44 , and 0.19 , with the remaining (negligible) probability being assigned to a *noise* class (e.g., main sequence). Moreover, application of the deep learning classification method of Hon et al. (2017, 2018), which uses folded background-corrected power spectra and $\Delta\nu$ as input, gives support to this by favoring an RGB scenario with high confidence ($p > 0.9$).

Finally, we assessed the evolutionary state of ι Dra based on a preliminary grid-based modeling exercise, having considered as observational constraints its global oscillation parameters, T_{eff} , $[\text{Fe}/\text{H}]$, and a parallax-based luminosity (see Table 1). We modeled the star twice, assuming it is either on the RGB or in the red clump (RC). We found that the global likelihood of the star being on the RGB is several orders of magnitude higher than it being in the RC. Interpreting this in terms of a

Bayes' factor provides decisive evidence in favor of the RGB scenario given the adopted set of seismic and spectroscopic constraints. To test whether this conclusion is robust against the adopted spectroscopic constraints (cf. Campante et al. 2019), we also considered the T_{eff} and $[\text{Fe}/\text{H}]$ derived from high-resolution optical and near-infrared CARMENES spectra (see table A2 of Marfil et al. 2020), having obtained similar results.

4. DETAILED MODELING

This study makes use of two independent pipelines — hereafter labeled ‘TL’ and ‘JO’ — for the detailed modeling. We resort to the TL Pipeline to test the impact of the optimization procedure (Sect. 4.1), investigating how different sets of observed oscillation modes contribute to the characterization of the two HLRGB stars being considered. We next use the JO Pipeline to assess how the choice of model physics, more specifically, the atmospheric boundary condition, modifies the inferred stellar properties (Sect. 4.2). Since the two pipelines employ different underlying grids of stellar models, we are able to roughly characterize the relative importance of these methodological decisions (Sect. 4.3).

Besides KOI-3886 and ι Dra, we also model the benchmark HLRGB star KIC 8410637 (TIC 123417372, TYC 3130-2385-1; Frandsen et al. 2013; Gaulme et al. 2016; Li et al. 2018, 2022; Themeßl et al. 2018), for which multi-year *Kepler* time-series photometry is available. This star was selected both for having a ν_{max} similar to that of KOI-3886 and ι Dra, as well as for being in an (detached) eclipsing binary. Owing to the latter feature, its mass and radius have been accurately determined via the dynamical modeling of the eclipsing binary's orbit (Frandsen et al. 2013), and can thus provide a direct test to the seismic determination. Observed mode frequencies for KIC 8410637 are taken from table A2 of Li et al. (2018). We also note that a precise (0.5%) interferometric radius is available for ι Dra (Baines et al. 2011), hence providing an additional test. These *reference* fundamental stellar properties are listed in Table 1.

4.1. Testing the Impact of the Optimization Procedure (TL Pipeline)

4.1.1. Stellar Models, Input Physics, and Grid Computation

We use the stellar evolution code MESA (Modules for Experiments in Stellar Astrophysics, release version 12115; Paxton et al. 2011, 2013, 2015, 2018) and the stellar oscillation code GYRE (v5.1; Townsend & Teitler 2013) to compute a grid of stellar models. We adopt the solar chemical mixture, $(Z/X)_{\odot} = 0.0181$, provided

by Asplund et al. (2009). The MESA ρ - T tables, based on the 2005 update of the OPAL equation of state tables (Rogers & Nayfonov 2002), are adopted and we use OPAL opacities supplemented by the low-temperature opacities from Ferguson et al. (2005). The MESA ‘simple’ photosphere is used for the set of boundary conditions for modeling the atmosphere, i.e., the opacity of the model atmosphere is specified by the temperature of the outermost mesh point of the interior model via a gray Eddington T - τ relation. The mixing-length theory of convection is applied, parameterized by α_{MLT} . We consider convective overshooting in the core, H-burning shell, and envelope. The exponential scheme by Herwig (2000) is applied. The overshoot parameter is mass-dependent and follows the relation $f_{\text{ov}} = [0.13 M(M_{\odot}) - 0.098]/9.0$ (Magic et al. 2010). For models with masses above $2.0 M_{\odot}$, we adopt a fixed f_{ov} of 0.018. For a smooth convective boundary, we also apply the MESA predictive mixing scheme. The mass-loss rate on the RGB is characterized by a Reimers' efficiency parameter (Reimers 1975) of $\eta = 0.2$, constrained by seismic targets in the old open clusters NGC 6791 and NGC 6819 (Miglio et al. 2012). Atomic diffusion is only considered for models with masses below $1.1 M_{\odot}$ during the main-sequence phase (it is turned off when the central hydrogen fraction falls below 0.01).

We compute a grid of models with masses ranging from 0.76 to $2.20 M_{\odot}$ and a step size of $0.02 M_{\odot}$. Besides the stellar mass, M , there are three other independent model inputs, namely, the initial helium fraction, Y_1 , the initial metallicity, $[\text{Fe}/\text{H}]_i$, and the mixing-length parameter, α_{MLT} . Model input ranges and step sizes are provided in Table 2. We evolve stellar evolutionary tracks from the Hayashi line and terminate them either when $\log g \leq 1.5$ dex on the RGB or helium-core burning starts (corresponding to an increase in the core heavy-element fraction).

4.1.2. Optimization

The fitting scheme is based on a maximum likelihood estimation (MLE) approach and is described in detail in Li et al. (2020). We adopt the spectroscopic T_{eff} and $[\text{Fe}/\text{H}]$ as classical constraints. A luminosity constraint is also adopted, although only in the cases of KOI-3886 and ι Dra. KIC 8410637 is in an eclipsing binary, which can potentially give rise to a biased estimate of the absolute luminosity, that being the reason why we opt for not imposing a luminosity constraint for this star. The fitting scheme employs the two-term surface correction method of Ball & Gizon (2014) and further considers a model systematic uncertainty, which is estimated as the median frequency difference between observations and

Table 2. Model grids: Input ranges, step sizes, and main differences in terms of the input physics.

Input Parameters	TL Pipeline			JO Pipeline ^a	
	From	To	Step	From	To
M (M_{\odot})	0.76	2.20	0.02	1.2	2.0
$[\text{Fe}/\text{H}]_i$ (dex)	-0.5	0.5	0.1	-0.4	0.4
Y_i	0.24	0.32	0.02	0.25	0.32
α_{MLT}	1.7	2.5	0.2	1.55	1.95
Chemical Mixture	Asplund et al. (2009)			Grevesse & Sauval (1998)	
Overshooting	Mass-dependent			None	
Model Atmosphere	‘Simple’			Varies	
Surface Correction ^b	Ball & Gizon (2014)			Roxburgh (2016)	

^aStep sizes undefined as stellar models were computed over a pseudorandomly sampled mesh of input parameters.

^bConcerns the optimization procedure rather than the input physics.

431 the best-fitting model. Moreover, mode frequencies are
 432 re-weighted as a function of their frequency difference
 433 with respect to ν_{max} when calculating the likelihood.

434 We test three optimization procedures. The differ-
 435 ences between procedures have solely to do with the seis-
 436 mic constraints adopted. The first of these procedures
 437 only considers $\ell = 0$ modes; the second includes $\ell = 0$
 438 and 2 modes, as well as the most p-like $\ell = 1$ modes; and
 439 the third procedure makes use of all observed mode fre-
 440 quencies (which include g-dominated modes). We refer
 441 to these three procedures as methods ‘0’ (radial modes),
 442 ‘P’ (p-dominated modes), and ‘A’ (all modes), respec-
 443 tively. The most p-like dipole modes are manually se-
 444 lected (cf. Tables A1 and A2). Since these modes are
 445 p-dominated, they have relatively high amplitudes and
 446 large widths in the power spectrum. Moreover, their
 447 frequency pattern on an échelle diagram should exhibit
 448 a curvature similar to that of radial modes. We follow
 449 both these criteria in manually selecting the most p-like
 450 dipole modes.

451 4.1.3. Results and Discussion

452 Table 3 lists the estimated stellar properties (mass,
 453 radius, surface gravity, and age) stemming from each
 454 of the three optimization methods. This is comple-
 455 mented by Fig. 5, where the dynamical mass and radius
 456 of KIC 8410637, as well as the interferometric radius of
 457 ι Dra are also represented. Figure 6 shows the best-
 458 fitting models (method ‘A’) on an échelle diagram as
 459 well as the probability distributions (all three methods)
 460 for the stellar mass.

461 We are able to accurately retrieve (i.e., within the
 462 quoted measurement uncertainties) the available *refer-*
 463 *ence* stellar properties using each of the optimization
 464 methods (see Fig. 5). Inspection of the mass probability
 465 distributions (see Fig. 6) further reveals that the esti-
 466 mates returned by the different optimization methods

467 are consistent within 1σ for all three stars (a statement
 468 that holds true when applied to the remaining stellar
 469 properties, as can be seen in Fig. 5).

470 Radial modes alone (method ‘0’) are capable of pre-
 471 cisely constraining the stellar properties, reaching a pre-
 472 cision of 2.4–3.5%, 6–10%, and 23–28% on the radius,
 473 mass, and age, respectively (cf. Li et al. 2022). The in-
 474 clusion of $\ell = 1$ and 2 modes in the fitting process (meth-
 475 ods ‘P’ and ‘A’) leads to a marginal gain in precision at
 476 best for both KOI-3886 and ι Dra. For KIC 8410637,
 477 the extra constraints provided by these modes lead to a
 478 more noticeable improvement not only in the precision
 479 (e.g., 5.8% on the mass with method ‘P’ versus 10%
 480 with method ‘0’) but also in the accuracy of the stellar
 481 property estimates (e.g., a mass accurate within 1.3%
 482 with method ‘P’ versus 7.7% with method ‘0’). Overall,
 483 a precision of 1.8–3.0%, 5–9%, and 19–25% respectively
 484 on the radius, mass, and age is attained with method
 485 ‘P’. We note that these are relatively low-mass stars
 486 — eventually igniting helium in the core in degener-
 487 ate conditions — and thus have core conditions that do
 488 not vary significantly. This can be used to explain why
 489 the impact of including seismic indicators that probe
 490 the core (i.e., $\ell = 1$ g-dominated modes as well as the
 491 combination of $\ell = 0$ and 2 modes) is limited. This
 492 is illustrated, for instance, in figs. 4 and 5 of Lagarde
 493 et al. (2016), where the mass dependence of $\Delta\Pi_1$ near
 494 the luminosity bump can be seen to almost vanish for
 495 $M \lesssim 1.8M_{\odot}$. The mass dependence of $\Delta\Pi_1$ thus ef-
 496 fectively becomes commensurate with the characteristic
 497 uncertainties, i.e., including statistical and systematic⁵

⁵ For reference, the model systematic uncertainty for KIC 8410637, estimated as the median frequency difference between observations and the best-fitting model (cf. Sect. 4.1.2), takes the values 0.012, 0.025, and 0.009 μHz for $\ell = 0, 1,$ and 2 modes, respectively.

498 contributions, on the observed frequencies for the stars
 499 in this study. This explanation holds true except per-
 500 haps where the mass approaches the degenerate transi-
 501 tion. This is most noticeable in the case of KIC 8410637,
 502 for which a luminosity constraint was not imposed, al-
 503 though KOI-3886 also has mass solutions above $1.8 M_{\odot}$
 504 that are not removed when including the $\ell = 1$ modes
 505 (see Fig. 5).

506 Moreover, we do not find significant differences be-
 507 tween methods ‘P’ and ‘A’ in all three cases, i.e., g-
 508 dominated dipole mixed modes seem not to provide ex-
 509 tra constraints on the inferred stellar properties. By
 510 inspecting the mode frequencies of the best-fitting mod-
 511 els (see Fig. 6), we notice that these HLRGB stars have
 512 very densely spaced dipole mixed modes, with a very
 513 small period spacing in the underlying g modes. At
 514 the same time, not every g-dominated mixed mode in
 515 the neighborhood of a given p-dominated mixed mode
 516 is observationally available. If the g-mode spacing is suf-
 517 ficiently small, an arbitrary identification of the radial
 518 order for each mode may be adopted to fit the dense for-
 519 est of model g-dominated mode frequencies to the sparse
 520 set of observed modes (except perhaps at the highest
 521 frequencies, for which the spacing becomes larger than
 522 the characteristic uncertainties on the observed frequen-
 523 cies). The resulting posterior distribution for the mass is
 524 then highly multimodal (see, e.g., the mass distribution
 525 for KOI-3886 corresponding to method ‘A’ in Fig. 6),
 526 with each peak corresponding to a different choice of
 527 mode identification (cf. Ong & Basu 2020). This multi-
 528 modality may in principle be alleviated with an a priori
 529 identification of these mixed modes, e.g., through mea-
 530 surement of the g-mode spacing, $\Delta\Pi_1$.

531 Another aspect worth noting is that the precision
 532 achieved on the stellar properties is very similar across
 533 the three-star sample. Given that ι Dra is a TESS
 534 target with a much shorter temporal coverage (5 non-
 535 contiguous TESS sectors), it appears that having ac-
 536 cess to multi-year time-series photometry (resulting in
 537 a higher-resolution power spectrum) does not signifi-
 538 cantly improve on the detailed modeling results for this
 539 type of stars. As discussed above, since p-dominated
 540 mixed modes mostly constrain the stellar properties,
 541 those longer-lived g-dominated modes extracted from
 542 high-resolution power spectra become more of a redun-
 543 dancy in the fitting process. For this reason, we obtain
 544 similar precision on the stellar properties for the multi-
 545 sector TESS target ι Dra and the multi-year *Kepler* tar-
 546 gets KOI-3886 and KIC 8410637. We, however, stress
 547 that the temporal coverage is still critical for HLRGB
 548 stars, as it allows to robustly identify and measure (long-

549 lived) mixed modes, ultimately determining their relia-
 550 bility (cf. Sect. 3.2).

551 4.2. Testing the Impact of the Input Physics: Model 552 Atmosphere (JO Pipeline)

553 4.2.1. Stellar Models, Input Physics, and Grid 554 Computation

555 A different set of stellar models were generated with
 556 MESA release version 12778 using the relative elemental
 557 abundances of Grevesse & Sauval (1998), without ele-
 558 ment diffusion or convective overshooting, and permit-
 559 ting the initial helium abundances, initial metallicities,
 560 and mixing-length parameter to vary freely. A mass-loss
 561 rate characterized by a Reimers’ efficiency parameter of
 562 $\eta = 0.2$ was adopted, as in the previous section. We re-
 563 tain stellar models at a constant temporal spacing of 0.2
 564 Myr, starting from the point where $\nu^2 \Delta\Pi_1 / \Delta\nu = 5$ up
 565 to core helium exhaustion at the end of the horizontal
 566 branch phase of evolution.

567 Two model grids (grids ‘1’ and ‘2’) were constructed in
 568 this manner, although with a different treatment of the
 569 model atmosphere. Even if both model grids use pho-
 570 tospheric boundary conditions with respect to a gray
 571 atmosphere in the Eddington approximation, for grid
 572 ‘1’ the model mesh was extended outwards to an opti-
 573 cal depth of $\tau = 10^{-3}$ under spherical geometry (joined
 574 with a small plane-parallel section from $\tau = 10^{-4}$ to
 575 $\tau = 10^{-3}$), while in grid ‘2’ the photospheric bound-
 576 ary condition was integrated under plane-parallel geom-
 577 etry from an optical depth of $\tau = 10^{-3}$ to $\tau = \frac{4}{3}$, where it
 578 was joined with the inner spherical mesh. The latter
 579 boundary condition is the same as that used in the pre-
 580 vious section, except that here the atmospheric opacity
 581 is allowed to vary consistently with the local tempera-
 582 ture and pressure in the atmosphere, rather than being
 583 held fixed to the outermost cell of the interior model.

584 For either choice of input physics, we then computed
 585 stellar models over a pseudorandomly sampled mesh of
 586 initial parameters $\{M, [\text{Fe}/\text{H}]_i, Y_i, \alpha_{\text{MLT}}\}$. These val-
 587 ues were distributed uniformly over the intervals $M \in$
 588 $[1.2, 2.0] M_{\odot}$, $[\text{Fe}/\text{H}]_i \in [-0.4, 0.4]$ dex, $Y_i \in [0.25, 0.32]$,
 589 and $\alpha_{\text{MLT}} \in [1.55, 1.95]$ by sampling over this parameter
 590 space with respect to a joint Sobol sequence, 4000 ele-
 591 ments long. The initial mass and metallicity were twice
 592 as densely sampled as the other parameters, owing to
 593 the wide ranges spanned by these parameters.

594 4.2.2. Optimization

595 For sufficiently evolved red giants ($\Delta\nu \lesssim 5 \mu\text{Hz}$), the
 596 uncoupled π -mode frequencies of nonradial modes asso-
 597 ciated with stellar models may be used in lieu of mixed-
 598 mode frequencies to match the most p-dominated ob-
 599 served mixed modes (cf. Ong et al. 2021b), such that

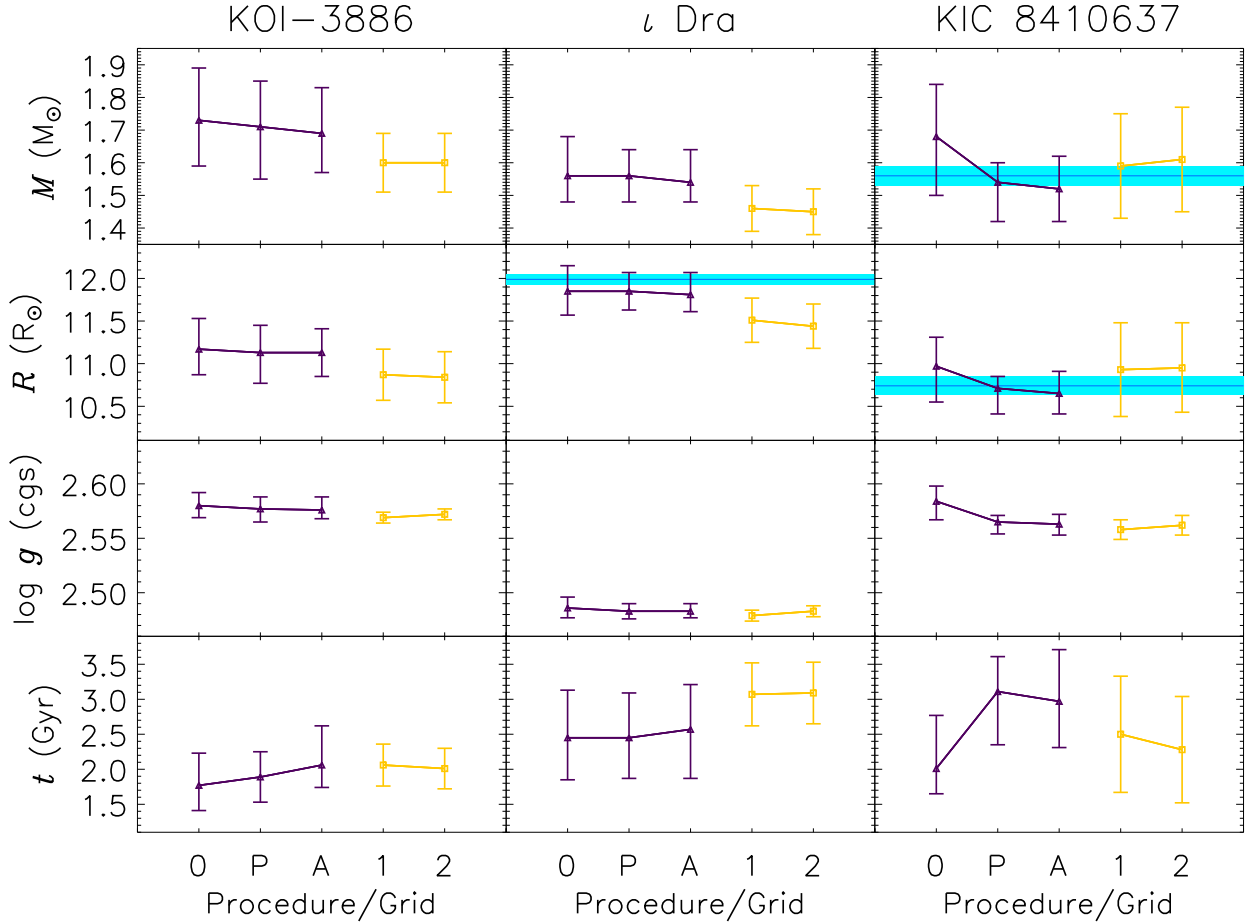


Figure 5. Estimated stellar properties for KOI-3886, ι Dra, and KIC 8410637. Detailed modeling results from the TL (dark purple) and JO (yellow) Pipelines are shown. Procedures/Grids are labeled as ‘0’, ‘P’, ‘A’ (cf. Sect. 4.1), and ‘1’, ‘2’ (cf. Sect. 4.2). Blue shaded areas represent the 1σ confidence intervals of the dynamical mass and radius of KIC 8410637, as well as of the interferometric radius of ι Dra.

600 the statistical error associated with the mode frequen-
 601 cies still dominates over any systematic errors caused
 602 by, e.g., an inappropriate surface-term correction. The
 603 numerical evaluation of these π modes is by far compu-
 604 tationally cheaper than for mixed modes and, for this
 605 reason, we hereafter restrict our attention to these p-
 606 dominated modes.

607 π -mode frequencies (in the sense of Ong & Basu 2020)
 608 were computed for $\ell = 0, 1$, and 2 modes within
 609 $\pm 4\Delta\nu$ of ν_{\max} . As in Ong et al. (2021a), we apply
 610 the ε_ℓ -matching algorithm of Roxburgh (2016) to yield
 611 a surface-independent discrepancy function, χ_ε^2 , on the
 612 internal structure from the mode frequencies. This al-
 613 gorithm operates by constructing diagnostic quantities
 614 out of both the model and observed mode frequencies,
 615 independently for each degree ℓ . Agreement with the
 616 internal structure of the model, insensitive to the stel-
 617 lar surface, is achieved when these quantities collapse
 618 to a single function of frequency, in principle minimiz-

619 ing χ_ε^2 when a nonparametric functional model is fitted
 620 against the data points. In order to permit the inclusion
 621 of the dipole modes in this procedure, the most p-like
 622 dipole mode was identified manually for each radial or-
 623 der and the associated frequency measurement error was
 624 inflated by adding in quadrature the local g-mode spac-
 625 ing, $\nu^2\Delta\Pi_1$, which was also estimated manually. While
 626 this mode selection was conducted independently of that
 627 in Sect. 4.1.2, almost exactly the same modes ended up
 628 being used here (cf. Tables A1 and A2). We chose to use
 629 the three lowest-frequency modes (without regard for
 630 degree) for the purpose of regularizing the ε_ℓ -matching
 631 algorithm, as described in Ong et al. (2021a).

632 For each model in the grid, we compute a likelihood
 633 function, $\mathcal{L} \sim \exp[-\chi^2/2]$, where the discrepancy func-
 634 tion, χ^2 , is comprised of several terms:

- 635 — χ_{glob}^2 , being the sum of error-normalized discrep-
 636 ancies for global properties, namely, the classical
 637 spectroscopic quantities T_{eff} and $[\text{Fe}/\text{H}]$, the lu-

Table 3. Estimated stellar properties for KOI-3886, ι Dra, and KIC 8410637 (TL Pipeline).

Star	M (M_{\odot})	R (R_{\odot})	$\log g$ (cgs)	t (Gyr)	Norm. RMS Dev. ^a	Seismic Constraints ^b
KOI-3886	$1.73^{+0.16}_{-0.14}$	$11.17^{+0.36}_{-0.30}$	$2.580^{+0.012}_{-0.011}$	$1.77^{+0.46}_{-0.36}$	0.21 (0.44)	0
	$1.71^{+0.14}_{-0.16}$	$11.13^{+0.32}_{-0.36}$	$2.577^{+0.011}_{-0.012}$	$1.89^{+0.36}_{-0.36}$	0.04 (0.25)	P
	$1.69^{+0.14}_{-0.12}$	$11.13^{+0.28}_{-0.28}$	$2.576^{+0.012}_{-0.008}$	$2.06^{+0.56}_{-0.32}$	0.21 (0.24)	A
ι Dra	$1.56^{+0.12}_{-0.08}$	$11.85^{+0.30}_{-0.28}$	$2.486^{+0.010}_{-0.009}$	$2.45^{+0.68}_{-0.60}$	0.12 (0.45)	0
	$1.56^{+0.08}_{-0.08}$	$11.85^{+0.22}_{-0.22}$	$2.483^{+0.007}_{-0.007}$	$2.45^{+0.64}_{-0.58}$	0.09 (0.51)	P
	$1.54^{+0.10}_{-0.06}$	$11.81^{+0.26}_{-0.20}$	$2.483^{+0.007}_{-0.006}$	$2.57^{+0.64}_{-0.70}$	0.14 (0.33)	A
KIC 8410637	$1.68^{+0.16}_{-0.18}$	$10.97^{+0.34}_{-0.42}$	$2.584^{+0.014}_{-0.017}$	$2.01^{+0.76}_{-0.36}$	0.84 (0.82)	0
	$1.54^{+0.06}_{-0.12}$	$10.71^{+0.14}_{-0.30}$	$2.565^{+0.006}_{-0.011}$	$3.11^{+0.50}_{-0.76}$	0.54 (0.59)	P
	$1.52^{+0.10}_{-0.10}$	$10.65^{+0.26}_{-0.24}$	$2.563^{+0.009}_{-0.010}$	$2.97^{+0.74}_{-0.66}$	0.60 (0.61)	A
				0.31 (0.47) [†]		

^aNormalized RMS deviation about the mean (d_{norm} ; see Eq. 1). Values outside (inside) brackets are computed considering mean property values across the set of procedures ‘0’, ‘P’, and ‘A’ (all procedures/grids, i.e., ‘0’, ‘P’, ‘A’, ‘1’, and ‘2’).

^b‘0’: $\ell = 0$ modes only; ‘P’: $\ell = 0$ and 2 modes, as well as most p-like $\ell = 1$ modes; ‘A’: All observed modes.

[†]Average value, $\langle d_{\text{norm}} \rangle$.

638 minosity (adopted only for KOI-3886 and ι Dra;
 639 cf. Sect. 4.1.2), and ν_{max} , computed from models
 640 using the scaling relation.

641 — χ^2_{ε} , which is the reduced χ^2 statistic returned by
 642 the nonparametric ε_{ℓ} -matching algorithm of Rox-
 643 burgh (2016).

644 — χ^2_{reg} , the regularization term describing the dis-
 645 crepancy for the three lowest-frequency modes.
 646 This term is downweighted by a factor of 4, so as
 647 not to unduly influence the shape of the posterior
 648 distribution.

649 With this likelihood function in hand, we then esti-
 650 mate probability distributions for the stellar properties
 651 using the Monte Carlo procedure described in Ong et al.
 652 (2021a). In summary, the posterior means for various
 653 properties are computed with respect to the likelihood
 654 function over the grid of models, normalized by the sam-
 655 pling function of the grid (to impose the assumption of
 656 uniform priors). This is done repeatedly with the likeli-
 657 hood function being re-evaluated under randomized per-
 658 turbations to the observable constraints, as specified by
 659 their nominal measurement errors. The resulting distri-
 660 bution of the posterior means is then used to report the
 661 values and uncertainties of the desired properties. While
 662 it would be prohibitively expensive — computationally
 663 speaking — to include perturbations to the mode fre-
 664 quencies, omitting their errors from this procedure has

665 been shown, for main-sequence stars at least, not to ap-
 666 precially affect the resulting posterior distributions, ex-
 667 cept that for the stellar age (cf. Cunha et al. 2021). In
 668 the case of red giants, however, their rapid evolution is
 669 such that their ages and masses are tightly correlated,
 670 and so this omission also leads to an underestimation of
 671 the uncertainties in properties other than the age. For
 672 this reason, we instead report, for each property, the
 673 quadratic mean of two different error estimates: the 1σ
 674 quantiles of the distribution of the posterior means (the
 675 usual approach), as well as the posterior standard devia-
 676 tion associated with a single realization of the procedure
 677 (representing the frequency uncertainties).

4.2.3. Results and Discussion

678
 679 We list in Table 4 the mass, radius, surface gravity,
 680 and age estimates returned by the above procedure for
 681 each star, as applied to the two model grids (see also
 682 Fig. 5). As in the previous section, we find very good
 683 agreement (i.e., within 1σ) between the results of this
 684 exercise and both the dynamical mass and radius of
 685 KIC 8410637. Agreement with the interferometric ra-
 686 dius of ι Dra is instead achieved within 2σ . The Monte
 687 Carlo procedure also allows estimating and comparing
 688 both the marginal and joint posterior distributions of
 689 the stellar properties, which we show in Figs. 7 to 9.
 690 Note, following our discussion above, that the widths
 691 of the distributions returned by the bootstrapping pro-
 692 cedure, which quantify the variations in the posterior

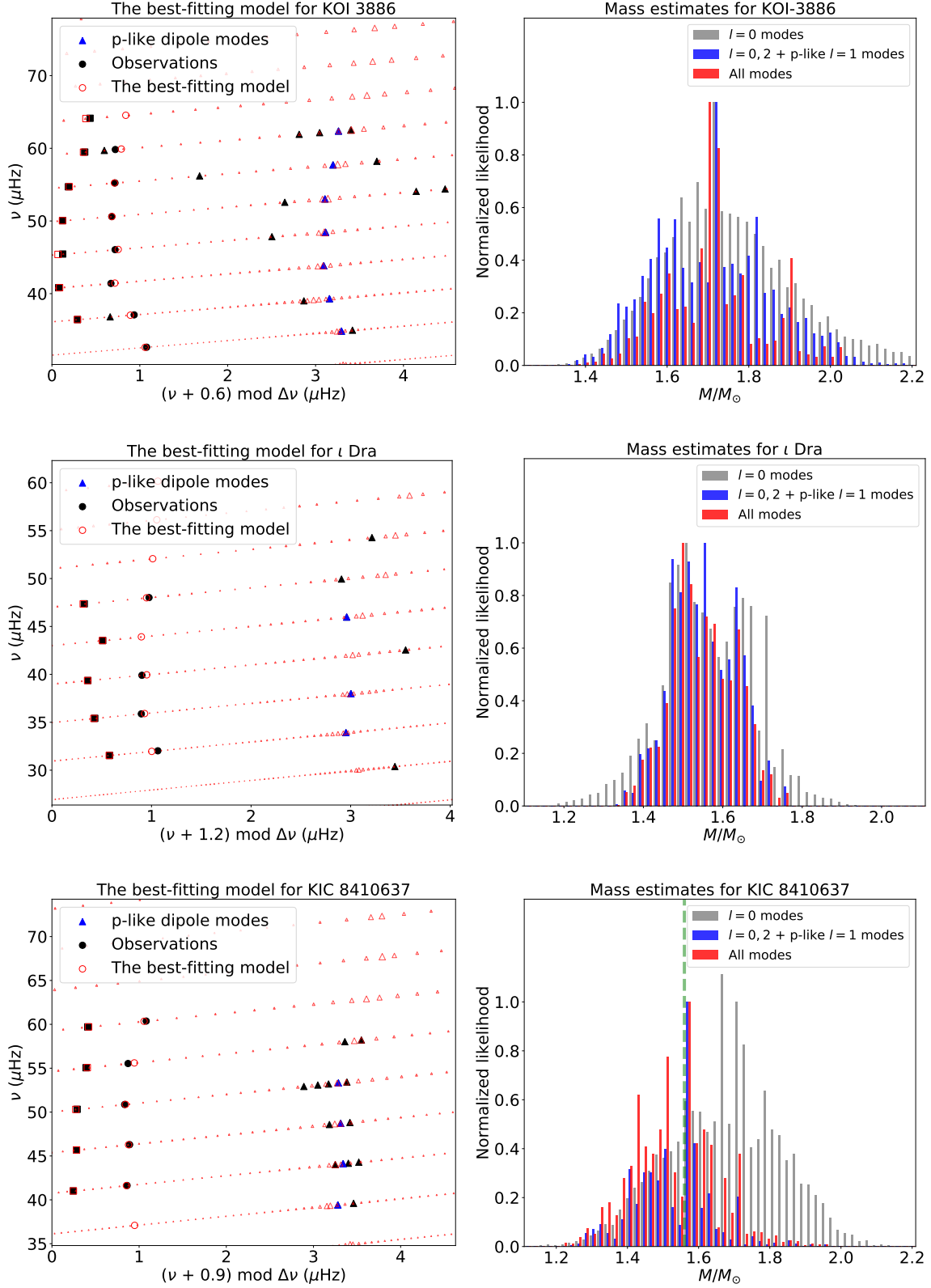


Figure 6. *Left Column:* Échelle diagrams of the best-fitting models for (from top to bottom) KOI-3886, ι Dra, and KIC 8410637 constrained by all the observed mode frequencies (method ‘A’). Circles, triangles, and squares represent $\ell = 0, 1,$ and 2 modes, respectively (the most p-like dipole modes are rendered in dark blue). A range of mixed $\ell = 1$ model frequencies are plotted with their symbol size scaled by the mode inertia (larger size means that the mode is more p-dominated). *Right Column:* Probability distributions for the stellar mass estimated using each of the three optimization methods (‘0’ in gray, ‘P’ in blue, and ‘A’ in red). The vertical dashed line in the bottom panel represents the dynamical mass of KIC 8410637.

mean under different realizations of the random error, are smaller than the reported uncertainties (these also include the posterior variances associated with individual realizations).

In Figs. 7 to 9, results corresponding to either choice of the atmospheric boundary condition are represented by the blue (grid ‘1’ or spherical atmosphere) and orange (grid ‘2’ or plane-parallel atmosphere) contours and histograms. We see marked differences in some of the inferred stellar properties. In particular, although the estimated masses and radii are not substantially changed relative to the reported uncertainties, the changes in the estimated mean densities (which combine them as $\rho \sim M/R^3$) are larger than the reported uncertainties for both KOI-3886 and ι Dra. This is likely in part because the mean density is constrained (albeit indirectly, via the seismic data) with an order of magnitude more relative precision than either M or R separately. On the other hand, this effect is not seen for KIC 8410637, for which a luminosity constraint was not adopted in this exercise. Since L is not imposed, changing the atmospheric boundary condition may allow the best-fitting model to have potentially a different luminosity (and therefore mass and age) in order to better satisfy the very tight $\Delta\nu$ constraint.

Aside from these statistical considerations, there are also significant physical and methodological implications associated with changing the atmospheric boundary condition. In terms of the spectroscopic observables, it is well-established that the choice of atmospheric boundary condition strongly determines the location of the RGB on the HR diagram associated with any given pair of Y_i , the initial helium abundance, and α_{MLT} , the mixing-length parameter. Accordingly, when the atmospheric boundary condition is changed, the values of Y_i and α_{MLT} that produce consistency with a fixed set of temperature and luminosity constraints must also be adjusted. Indeed, we see this happening in the bottom rows of Figs. 7 to 9, which show the joint and marginal distributions of Y_i for each of the three stars, where the value of Y_i that best describes each star is significantly modified (this is particularly noticeable in the case of ι Dra) between either choice of atmospheric boundary condition.

Changing the atmospheric boundary condition also modifies the mode frequencies of a stellar model (inducing a numerical seismic surface term). Existing methodological comparisons of surface term treatments for red giants (Ball et al. 2018; Jørgensen et al. 2020; Ong et al. 2021a), or even in general (Basu & Kinnane 2018; Compton et al. 2018; Nsamba et al. 2018), have usually considered the effects of different parameterizations of, or

corrections for, modeling errors in stellar surfaces, under numerical experiments in which these modeling errors (arising from how the underlying set of stellar models are being generated) are kept the same. In this case, however, we have performed a converse experiment: We have maintained the use of a single algorithm to mitigate the asteroseismic surface term throughout — the surface-independent ε_ℓ -matching scheme of Roxburgh (2016) — while changing the atmospheric boundary condition associated with the 1D evolutionary models. In particular, we have chosen a mitigation scheme that is designed to yield seismic constraints which are insensitive to the near-surface layers altogether, rather than attempting to correct their effects on the mode frequencies per se. Accordingly, the resulting systematics which we obtain originate from how the spectroscopic, rather than seismic, properties of the stellar models depend on the construction of their surface layers.

We see here that seismic estimates of mass and radius appear methodologically insensitive to the description of these near-surface layers, at the expense of substantially changing both the near-surface structure of the best-fitting models (i.e., changing the calibration constant in the scaling relation between $\Delta\nu$ and the mean density, which relies on homology arguments) and the values of associated parameters like the initial helium abundance (in tandem with the interaction with the spectroscopic constraints above). This means that attempts to measure Y_i from seismic modeling of red giants, e.g., for the purpose of Galactic chemical evolution (measuring dY/dZ relations) or Galactic archaeology studies, are systematically dependent on the choice of atmospheric boundary condition.

4.3. Intra- vs. Inter-pipeline Dispersion

Since the input physics underlying the TL and JO Pipelines differs in a number of aspects (cf. Table 2), a meaningful investigation of the source(s) of inter-pipeline systematics would not be possible. The exercises carried out in Sects. 4.1 and 4.2 should instead be regarded as independent, i.e., we are interested in assessing the intra- as opposed to the inter-pipeline dispersion.

We find it nonetheless instructive to roughly characterize the relative importance of the methodological choices made when operating each of these pipelines. To that end, we introduce a simple statistic, namely, the normalized root-mean-square (RMS) deviation about the mean:

$$d_{\text{norm}} = \sqrt{\frac{1}{4} \sum_i \left(\frac{p_i - \mu_{p_i}}{\sigma_i} \right)^2}, \quad (1)$$

Table 4. Estimated stellar properties for KOI-3886, ι Dra, and KIC 8410637 (JO Pipeline).

Star	M (M_{\odot})	R (R_{\odot})	$\log g$ (cgs)	t (Gyr)	Norm. RMS Dev. ^a	Model Grid ^b
KOI-3886	$1.60^{+0.09}_{-0.09}$	$10.87^{+0.30}_{-0.30}$	$2.569^{+0.005}_{-0.005}$	$2.06^{+0.30}_{-0.30}$	0.16 (0.75)	1
	$1.60^{+0.09}_{-0.09}$	$10.84^{+0.30}_{-0.30}$	$2.572^{+0.005}_{-0.005}$	$2.01^{+0.29}_{-0.29}$	0.16 (0.56)	2
ι Dra	$1.46^{+0.07}_{-0.07}$	$11.51^{+0.26}_{-0.26}$	$2.479^{+0.005}_{-0.005}$	$3.07^{+0.45}_{-0.45}$	0.21 (0.75)	1
	$1.45^{+0.07}_{-0.07}$	$11.44^{+0.26}_{-0.26}$	$2.483^{+0.005}_{-0.005}$	$3.09^{+0.44}_{-0.44}$	0.21 (0.78)	2
KIC 8410637	$1.59^{+0.16}_{-0.16}$	$10.93^{+0.55}_{-0.55}$	$2.558^{+0.009}_{-0.009}$	$2.50^{+0.83}_{-0.83}$	0.13 (0.48)	1
	$1.61^{+0.16}_{-0.16}$	$10.95^{+0.53}_{-0.52}$	$2.562^{+0.009}_{-0.009}$	$2.28^{+0.76}_{-0.76}$	0.14 (0.34)	2
					0.17 (0.61) [†]	

^aNormalized RMS deviation about the mean (d_{norm} ; see Eq. 1). Values outside (inside) brackets are computed considering mean property values across grids ‘1’ and ‘2’ (all procedures/grids, i.e., ‘0’, ‘P’, ‘A’, ‘1’, and ‘2’).

^b‘1’: Spherical atmosphere; ‘2’: Plane-parallel atmosphere. See Sect. 4.2.1 for details.

[†]Average value, $\langle d_{\text{norm}} \rangle$.

793 where p_i represents each of the four estimated stellar
794 properties (M , R , $\log g$, and t), σ_i is the associated un-
795 certainty, and μ_{p_i} is the property’s mean value across a
796 set of procedures/grids. We compute d_{norm} for each star
797 and procedure/grid combination and list it in Tables 3
798 and 4. Values outside brackets are computed considering
799 mean property values across the set of procedures/grids
800 within the same pipeline (i.e., TL or JO). Values inside
801 brackets are computed considering mean property values
802 across all procedures/grids (i.e., TL and JO combined).
803 Average values, $\langle d_{\text{norm}} \rangle$, are also provided, which can
804 be interpreted as proxies for the intra- and inter-pipeline
805 systematics, respectively. Figure 5 provides a visual aid.
806 Two features are worth noting. First, the inter-
807 pipeline systematics dominates over the intra-pipeline
808 systematics. This is more noticeable in the case of the
809 JO Pipeline, whose intra-pipeline systematics is a fac-
810 tor of ~ 2 smaller than for the TL Pipeline. Second,
811 the uncertainties on the stellar properties returned by
812 both pipelines are robust in the sense that their magni-
813 tudes are larger than the inter-pipeline (and hence intra-
814 pipeline) systematics, i.e., $\langle d_{\text{norm}} \rangle < 1$ everywhere.

815 5. SUMMARY AND CONCLUSIONS

816 We have conducted detailed asteroseismic modeling
817 of the HLRGB host stars KOI-3886 and ι Dra, mak-
818 ing use of two independent pipelines. A third star,
819 KIC 8410637, a member of an eclipsing binary, was also
820 modeled and used as benchmark. Multi-year *Kepler*
821 time-series photometry is available for both KOI-3886
822 and KIC 8410637, whereas multi-sector TESS time-
823 series photometry is available for ι Dra (ι Dra is, fur-
824 thermore, a saturated target in the TESS photometry).

825 Using one of the pipelines (TL Pipeline; Sect. 4.1),
826 we first tested the impact of the optimization procedure
827 by adopting different sets of observed oscillation modes
828 as seismic constraints, namely, radial modes (method
829 ‘0’), p-dominated modes (method ‘P’), and all modes
830 (method ‘A’). The main outcomes of this exercise are as
831 follows:

- 832 — Radial modes alone (method ‘0’) are capable of
833 accurately and precisely constraining the stellar
834 properties. A precision of 2.4–3.5%, 6–10%, and
835 23–28% respectively on the radius, mass, and age
836 is thus attained (cf. Li et al. 2022). Inclusion of
837 $\ell = 1$ and 2 modes (methods ‘P’ and ‘A’) im-
838 proves precision only marginally, with 1.8–3.0%,
839 5–9%, and 19–25% being reached when $\ell = 0$ and
840 2 modes, as well as the most p-like $\ell = 1$ modes,
841 are used as constraints (i.e., method ‘P’). The lim-
842 ited impact of including seismic probes to the core
843 of these relatively low-mass stars ($M \lesssim 1.8 M_{\odot}$)
844 can be explained by the fact that their core condi-
845 tions do not vary significantly, as attested by the
846 vanishing mass dependence of $\Delta\Pi_1$ near the lumi-
847 nosity bump (cf. Lagarde et al. 2016).

- 848 — Given the very small period spacing of dipole
849 mixed modes characteristic of HLRGB stars, a
850 sparse set of observed g-dominated dipole modes
851 does not provide extra constraints on the inferred
852 stellar properties. This happens, since an arbi-
853 trary identification of the radial order for each
854 mode may be adopted to fit the dense forest of
855 model g-dominated mode frequencies, resulting in
856 posterior distributions for the stellar mass that are

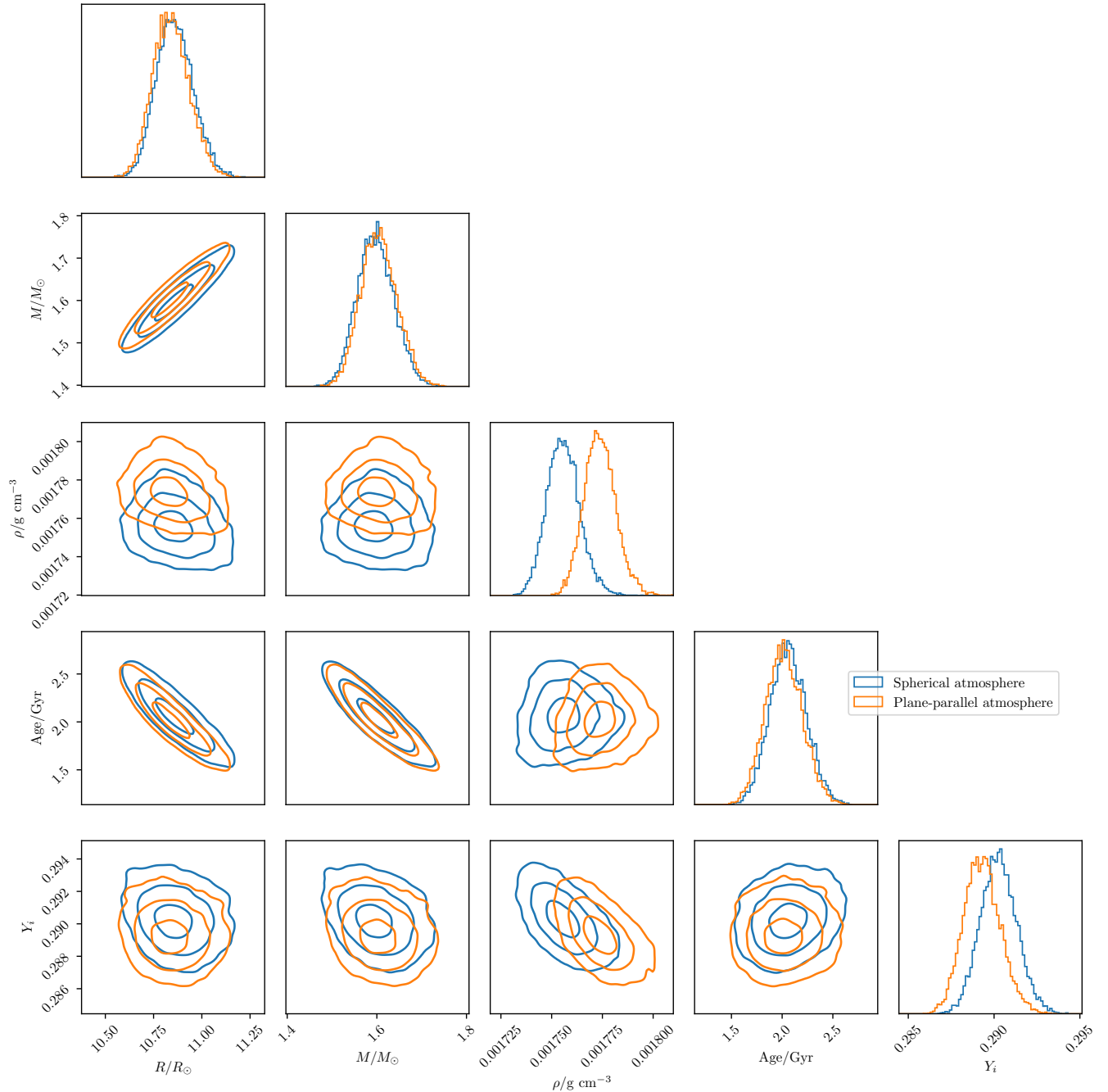


Figure 7. Joint posterior distribution of the stellar properties for KOI-3886, showing a comparison between either choice of physics in the underlying grids of evolutionary models.

857 highly multimodal (cf. Ong & Basu 2020). In principle, this multimodality may be alleviated by supplying an a priori identification for the radial orders of the observed mixed modes. In practice, however, doing so would require both accurate estimation of $\Delta\Pi_\ell$, as well as constraints on allowable values for the g-mode phase function, ε_g , near ν_{\max} . Such constraints may be provided, for exam-

855 ple, by JWKB analysis of the g-mode cavity when the star is significantly more or significantly less evolved than the RGB luminosity bump (Pinçon et al. 2019), or by homology relations in stars with degenerate helium cores (Deheuvels et al. 2021) given $\Delta\Pi_\ell$. However, more general considerations may require further theoretical investigation.

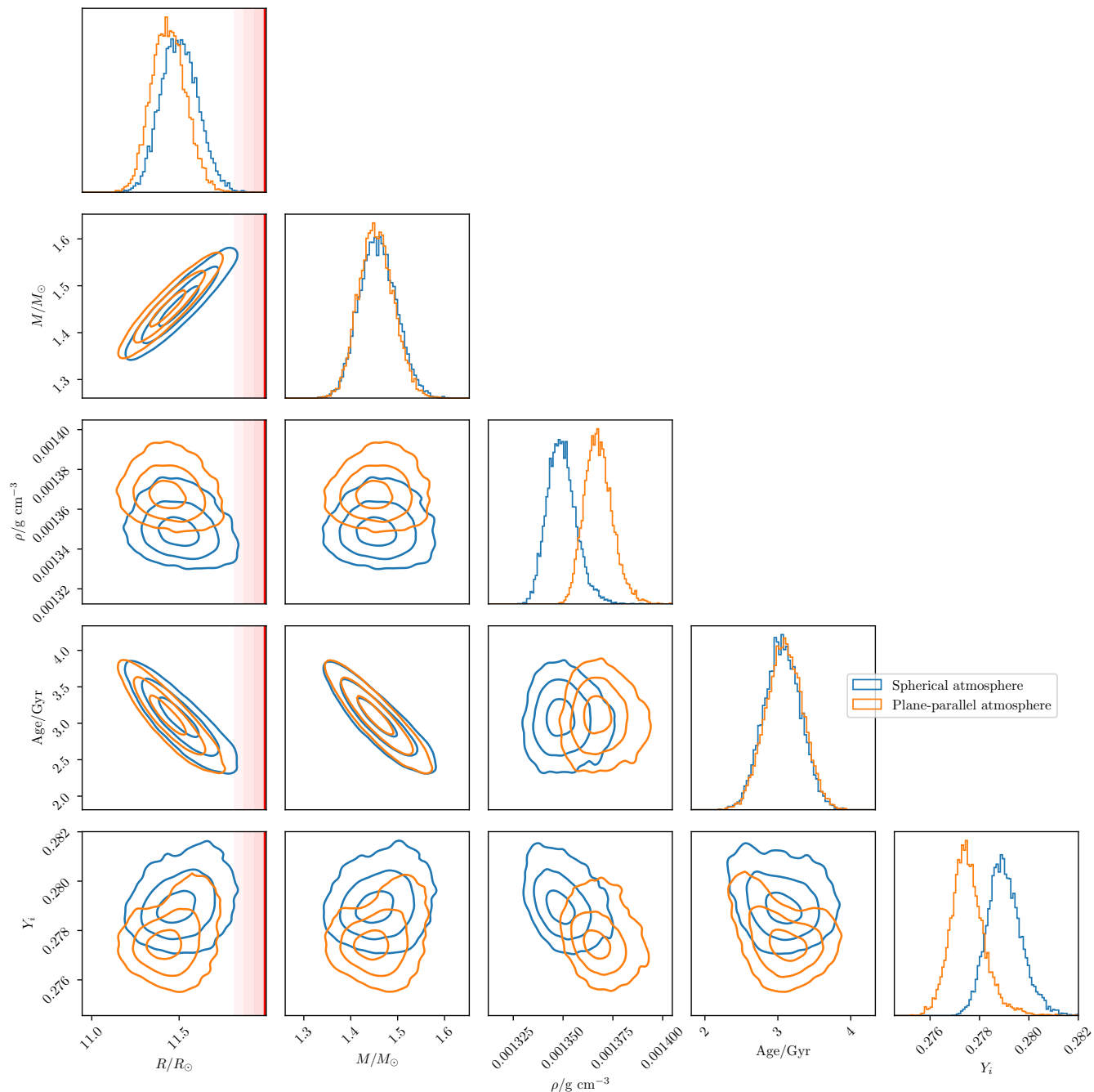


Figure 8. Joint posterior distribution of the stellar properties for ι Dra, showing a comparison between either choice of physics in the underlying grids of evolutionary models. The interferometric radius from Baines et al. (2011), as well as its associated uncertainty (1σ , 2σ , and 3σ), are depicted by the vertical line and shaded region, respectively.

872 — For the reasons stated above, shorter-lived p-
 873 dominated mixed modes end up mostly constrain-
 874 ing the stellar properties of HLRGB stars. There-
 875 fore, despite the much shorter temporal coverage
 876 (and thus lower resolution of the power spectrum)
 877 available for TESS targets compared to multi-year

878 *Kepler* observations, detailed modeling of the for-
 879 mer can lead to similarly precise stellar properties.

880 Next, using the other pipeline (JO Pipeline; Sect. 4.2),
 881 we tested the impact of the model physics, namely, the
 882 atmospheric boundary condition, on the inferred stellar
 883 properties. Changing the atmospheric boundary condi-
 884 tion is known to substantially modify the asteroseismic

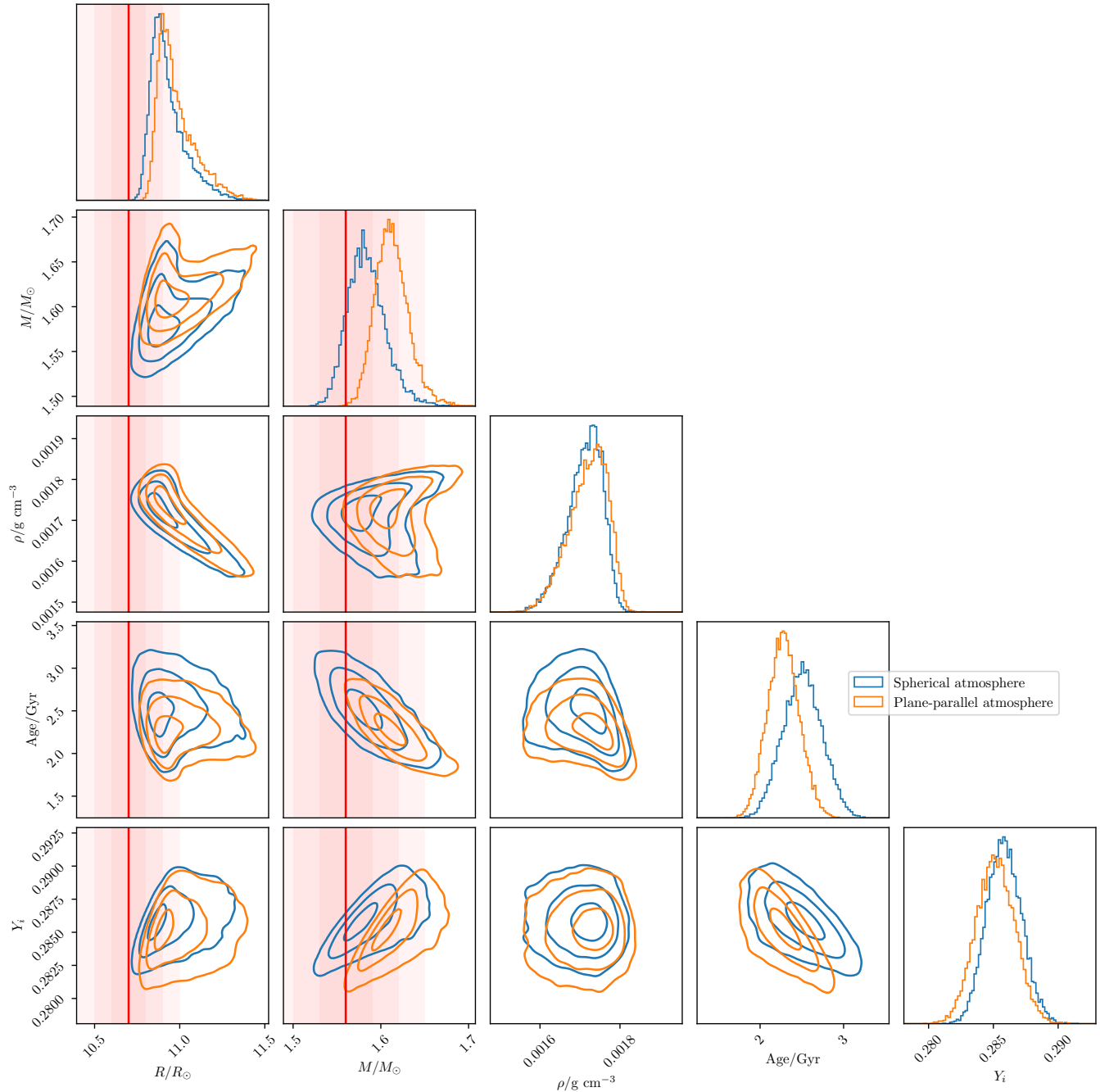


Figure 9. Joint posterior distribution of the stellar properties for KIC 8410637, showing a comparison between either choice of physics in the underlying grids of evolutionary models. The dynamical mass and radius from Frandsen et al. (2013), as well as their associated uncertainties (1σ , 2σ , and 3σ), are depicted by the vertical lines and shaded regions, respectively.

885 surface term — the differences in the mode frequencies
 886 between those of a star and a stellar model with identical
 887 interior structure, owing to modeling errors in the
 888 near-surface layers. Since these mode frequencies are
 889 measured far more precisely than the spectroscopic con-
 890 straints, this surface term is typically assumed to domi-
 891 nate the systematic error when estimating stellar prop-

892 erties, if left uncorrected or corrected inappropriately.
 893 However, we have shown that even when using a seis-
 894 mic constraint designed to be independent of the near-
 895 surface structure of stellar models, inferences of stel-
 896 lar properties are still significantly dependent on choices
 897 of atmospheric physics, as the spectroscopic properties

of the models are also modified by changing the atmospheric boundary condition.

This paper includes data collected by the *Kepler* and TESS missions. Funding for the *Kepler* and TESS missions is provided by the NASA Science Mission Directorate. This work was supported by Fundação para a Ciência e a Tecnologia (FCT) through research grants UIDB/04434/2020 and UIDP/04434/2020. T.L.C. is supported by FCT in the form of a work contract (CEECIND/00476/2018). J.M.J.O. was partially supported by NASA grant 80NSSC19K0374 awarded to Sarbani Basu. We thank the Yale Center for Research Computing for guidance and use of the research computing infrastructure.

Facilities: *Kepler*, TESS, *Gaia*.

Software: KEPSEISMIC (<https://archive.stsci.edu/prepds/kepseismic/>), KADACS (García et al. 2011, 2014; Pires et al. 2015), DIAMONDS (Corsaro & De Ridder 2014), FAMED (Corsaro et al. 2020), MESA (Paxton et al. 2011, 2013, 2015, 2018), GYRE (Townsend & Teitler 2013).

APPENDIX

A. FREQUENCY LISTS AND PEAK-BAGGING

REFERENCES

- Aizenman, M., Smeyers, P., & Weigert, A. 1977, *A&A*, 58, 41
- Asplund, M., Grevesse, N., Sauval, A. J., & Scott, P. 2009, *Annual Review of Astronomy and Astrophysics*, 47, 481, doi: [10.1146/annurev.astro.46.060407.145222](https://doi.org/10.1146/annurev.astro.46.060407.145222)
- Baines, E. K., McAlister, H. A., ten Brummelaar, T. A., et al. 2011, *ApJ*, 743, 130, doi: [10.1088/0004-637X/743/2/130](https://doi.org/10.1088/0004-637X/743/2/130)
- Ball, W. H., & Gizon, L. 2014, *A&A*, 568, A123, doi: [10.1051/0004-6361/201424325](https://doi.org/10.1051/0004-6361/201424325)
- Ball, W. H., Themeßl, N., & Hekker, S. 2018, *MNRAS*, 478, 4697, doi: [10.1093/mnras/sty1141](https://doi.org/10.1093/mnras/sty1141)
- Ball, W. H., Chaplin, W. J., Nielsen, M. B., et al. 2020, *MNRAS*, 499, 6084, doi: [10.1093/mnras/staa3190](https://doi.org/10.1093/mnras/staa3190)
- Basu, S., & Kinnane, A. 2018, *ApJ*, 869, 8, doi: [10.3847/1538-4357/aae922](https://doi.org/10.3847/1538-4357/aae922)
- Bedding, T. R., Mosser, B., Huber, D., et al. 2011, *Nature*, 471, 608, doi: [10.1038/nature09935](https://doi.org/10.1038/nature09935)
- Borucki, W. J., Koch, D. G., Basri, G., et al. 2010, *Science*, 327, 977, doi: [10.1126/science.1185402](https://doi.org/10.1126/science.1185402)
- Campante, T. L., Santos, N. C., & Monteiro, M. J. P. F. G., eds. 2018, *Astrophysics and Space Science Proceedings*, Vol. 49, *Asteroseismology and Exoplanets: Listening to the Stars and Searching for New Worlds* (Springer International Publishing), doi: [10.1007/978-3-319-59315-9](https://doi.org/10.1007/978-3-319-59315-9)
- Campante, T. L., Handberg, R., Mathur, S., et al. 2011, *A&A*, 534, A6, doi: [10.1051/0004-6361/201116620](https://doi.org/10.1051/0004-6361/201116620)
- Campante, T. L., Schofield, M., Kuszlewicz, J. S., et al. 2016, *ApJ*, 830, 138, doi: [10.3847/0004-637X/830/2/138](https://doi.org/10.3847/0004-637X/830/2/138)
- Campante, T. L., Veras, D., North, T. S. H., et al. 2017, *MNRAS*, 469, 1360, doi: [10.1093/mnras/stx876](https://doi.org/10.1093/mnras/stx876)
- Campante, T. L., Corsaro, E., Lund, M. N., et al. 2019, *ApJ*, 885, 31, doi: [10.3847/1538-4357/ab44a8](https://doi.org/10.3847/1538-4357/ab44a8)
- Christensen-Dalsgaard, J., Silva Aguirre, V., Elsworth, Y., & Hekker, S. 2014, *MNRAS*, 445, 3685, doi: [10.1093/mnras/stu2007](https://doi.org/10.1093/mnras/stu2007)
- Christensen-Dalsgaard, J., Silva Aguirre, V., Cassisi, S., et al. 2020, *A&A*, 635, A165, doi: [10.1051/0004-6361/201936766](https://doi.org/10.1051/0004-6361/201936766)
- Compton, D. L., Bedding, T. R., Ball, W. H., et al. 2018, *MNRAS*, 479, 4416, doi: [10.1093/mnras/sty1632](https://doi.org/10.1093/mnras/sty1632)
- Corsaro, E., & De Ridder, J. 2014, *A&A*, 571, A71, doi: [10.1051/0004-6361/201424181](https://doi.org/10.1051/0004-6361/201424181)
- Corsaro, E., McKeever, J. M., & Kuszlewicz, J. S. 2020, *A&A*, 640, A130, doi: [10.1051/0004-6361/202037930](https://doi.org/10.1051/0004-6361/202037930)
- Cunha, M. S., Roxburgh, I. W., Aguirre Børsen-Koch, V., et al. 2021, *MNRAS*, 508, 5864, doi: [10.1093/mnras/stab2886](https://doi.org/10.1093/mnras/stab2886)
- Davies, G. R., Handberg, R., Miglio, A., et al. 2014, *MNRAS*, 445, L94, doi: [10.1093/mnras/lu143](https://doi.org/10.1093/mnras/lu143)

Table A1. Extracted mode frequencies for KOI-3886.

n_p	ℓ	Frequency (μHz)	1σ Uncertainty (μHz)	p_{det}
6	0	32.629	0.047	1.000
6	1 ^{†,‡}	34.846	0.021	0.996
6	1	34.971	0.031	1.000
6	2	36.434	0.065	1.000
6	1	36.806	0.012	0.996
7	0	37.080	0.036	1.000
7	1	39.011	0.044	1.000
7	1 ^{†,‡}	39.302	0.042	—
7	2	40.813	0.057	1.000
8	0	41.408	0.065	—
8	1 ^{†,‡}	43.830	0.041	—
8	2	45.452	0.057	—
9	0	46.049	0.057	—
9	1	47.833	0.038	0.999
9	1 ^{†,‡}	48.444	0.045	—
9	2	50.045	0.070	—
10	0	50.604	0.063	—
10	1	52.573	0.030	1.000
10	1 ^{†,‡}	53.030	0.041	—
10	1	54.068	0.021	1.000
10	1	54.397	0.035	1.000
10	2	54.703	0.046	—
11	0	55.233	0.068	—
11	1	56.196	0.078	0.994
11	1 ^{†,‡}	57.715	0.061	—
11	1	58.213	0.033	1.000
11	2	59.482	0.061	1.000
11	1	59.705	0.026	1.000
12	0	59.830	0.025	1.000
12	1	61.922	0.006	0.993
12	1	62.155	0.025	0.998
12	1 ^{†,‡}	62.370	0.011	1.000
12	1	62.509	0.015	0.997
12	2	64.136	0.100	1.000

[†] Manually selected p-like dipole modes (see Sect. 4.1.2).

[‡] Manually selected p-like dipole modes (see Sect. 4.2.2).

972 Deheuvels, S., Ballot, J., Gehan, C., & Mosser, B. 2021,
973 arXiv e-prints, arXiv:2108.11848.
974 <https://arxiv.org/abs/2108.11848>
975 Elsworth, Y., Hekker, S., Basu, S., & Davies, G. R. 2017,
976 MNRAS, 466, 3344, doi: [10.1093/mnras/stw3288](https://doi.org/10.1093/mnras/stw3288)
977 Ferguson, J. W., Alexander, D. R., Allard, F., et al. 2005,
978 ApJ, 623, 585, doi: [10.1086/428642](https://doi.org/10.1086/428642)

979 Frandsen, S., Lehmann, H., Hekker, S., et al. 2013, A&A,
980 556, A138, doi: [10.1051/0004-6361/201321817](https://doi.org/10.1051/0004-6361/201321817)
981 Frink, S., Mitchell, D. S., Quirrenbach, A., et al. 2002, ApJ,
982 576, 478, doi: [10.1086/341629](https://doi.org/10.1086/341629)
983 Gaia Collaboration, Brown, A. G. A., Vallenari, A., et al.
984 2021, A&A, 649, A1, doi: [10.1051/0004-6361/202039657](https://doi.org/10.1051/0004-6361/202039657)
985 García, R. A., Hekker, S., Stello, D., et al. 2011, MNRAS,
986 414, L6, doi: [10.1111/j.1745-3933.2011.01042.x](https://doi.org/10.1111/j.1745-3933.2011.01042.x)

Table A2. Extracted mode frequencies for ι Dra.

n_p	ℓ	Frequency (μHz)	1σ Uncertainty (μHz)	p_{det}	List ^a
6	1	30.384	0.028	0.997	Min.
6	2	31.538	0.133	1.000	Min.
7	0	32.024	0.024	0.998	Min.
7	1 ^{†,‡}	33.913	0.088	1.000	Min.
7	2	35.410	0.039	—	Min.
8	0	35.878	0.035	—	Min.
8	1 ^{†,‡}	37.983	0.035	—	Min.
8	2	39.361	0.072	—	Min.
9	0	39.904	0.049	—	Min.
8	3	40.684	0.056	1.000	Max.
9	1	42.078	0.024	—	Max.
9	1	42.552	0.016	—	Min.
9	1	43.063	0.011	—	Max.
9	2	43.530	0.107	—	Min.
10	0	43.925	0.016	—	Max.
10	1 ^{†,‡}	45.980	0.027	—	Min.
10	2	47.364	0.072	—	Min.
11	0	48.015	0.038	—	Min.
11	1 [‡]	49.948	0.027	—	Min.
11	1	50.420	0.022	0.997	Max.
12	1	54.274	0.021	0.999	Min.
12	2	55.202	0.100	0.999	Max.
13	0	55.565	0.025	0.994	Max.

^a‘Min.’ = Belongs to Minimal List; ‘Max.’ = Belongs to Maximal List (but not to Minimal List). See Sect. 3.2 for a definition of both lists.

[†]Manually selected p-like dipole modes (see Sect. 4.1.2).

[‡]Manually selected p-like dipole modes (see Sect. 4.2.2).

987 García, R. A., Mathur, S., Pires, S., et al. 2014, *A&A*, 568,
988 A10, doi: [10.1051/0004-6361/201323326](https://doi.org/10.1051/0004-6361/201323326)
989 Gaulme, P., McKeever, J., Jackiewicz, J., et al. 2016, *ApJ*,
990 832, 121, doi: [10.3847/0004-637X/832/2/121](https://doi.org/10.3847/0004-637X/832/2/121)
991 Grevesse, N., & Sauval, A. J. 1998, *SSRv*, 85, 161,
992 doi: [10.1023/A:1005161325181](https://doi.org/10.1023/A:1005161325181)
993 Grunblatt, S. K., Huber, D., Gaidos, E., et al. 2019, *AJ*,
994 158, 227, doi: [10.3847/1538-3881/ab4c35](https://doi.org/10.3847/1538-3881/ab4c35)
995 —. 2017, *AJ*, 154, 254, doi: [10.3847/1538-3881/aa932d](https://doi.org/10.3847/1538-3881/aa932d)
996 Grunblatt, S. K., Saunders, N., Sun, M., et al. 2022, *AJ*,
997 163, 120, doi: [10.3847/1538-3881/ac4972](https://doi.org/10.3847/1538-3881/ac4972)
998 Handberg, R., & Campante, T. L. 2011, *A&A*, 527, A56,
999 doi: [10.1051/0004-6361/201015451](https://doi.org/10.1051/0004-6361/201015451)
1000 Herwig, F. 2000, *A&A*, 360, 952.
1001 <https://arxiv.org/abs/astro-ph/0007139>
1002 Hill, M. L., Kane, S. R., Campante, T. L., et al. 2021, *AJ*,
1003 162, 211, doi: [10.3847/1538-3881/ac1b31](https://doi.org/10.3847/1538-3881/ac1b31)

1004 Hon, M., Stello, D., & Yu, J. 2017, *MNRAS*, 469, 4578,
1005 doi: [10.1093/mnras/stx1174](https://doi.org/10.1093/mnras/stx1174)
1006 —. 2018, *MNRAS*, 476, 3233, doi: [10.1093/mnras/sty483](https://doi.org/10.1093/mnras/sty483)
1007 Howell, S. B., Sobeck, C., Haas, M., et al. 2014, *PASP*, 126,
1008 398, doi: [10.1086/676406](https://doi.org/10.1086/676406)
1009 Huber, D., Stello, D., Bedding, T. R., et al. 2009,
1010 *Communications in Asteroseismology*, 160, 74.
1011 <https://arxiv.org/abs/0910.2764>
1012 Huber, D., Chaplin, W. J., Chontos, A., et al. 2019, *AJ*,
1013 157, 245, doi: [10.3847/1538-3881/ab1488](https://doi.org/10.3847/1538-3881/ab1488)
1014 Jiang, C., Bedding, T. R., Stassun, K. G., et al. 2020, *ApJ*,
1015 896, 65, doi: [10.3847/1538-4357/ab8f29](https://doi.org/10.3847/1538-4357/ab8f29)
1016 Jofré, E., Petrucci, R., Saffe, C., et al. 2015, *A&A*, 574,
1017 A50, doi: [10.1051/0004-6361/201424474](https://doi.org/10.1051/0004-6361/201424474)
1018 Jørgensen, A. C. S., Montalbán, J., Miglio, A., et al. 2020,
1019 *MNRAS*, 495, 4965, doi: [10.1093/mnras/staa1480](https://doi.org/10.1093/mnras/staa1480)

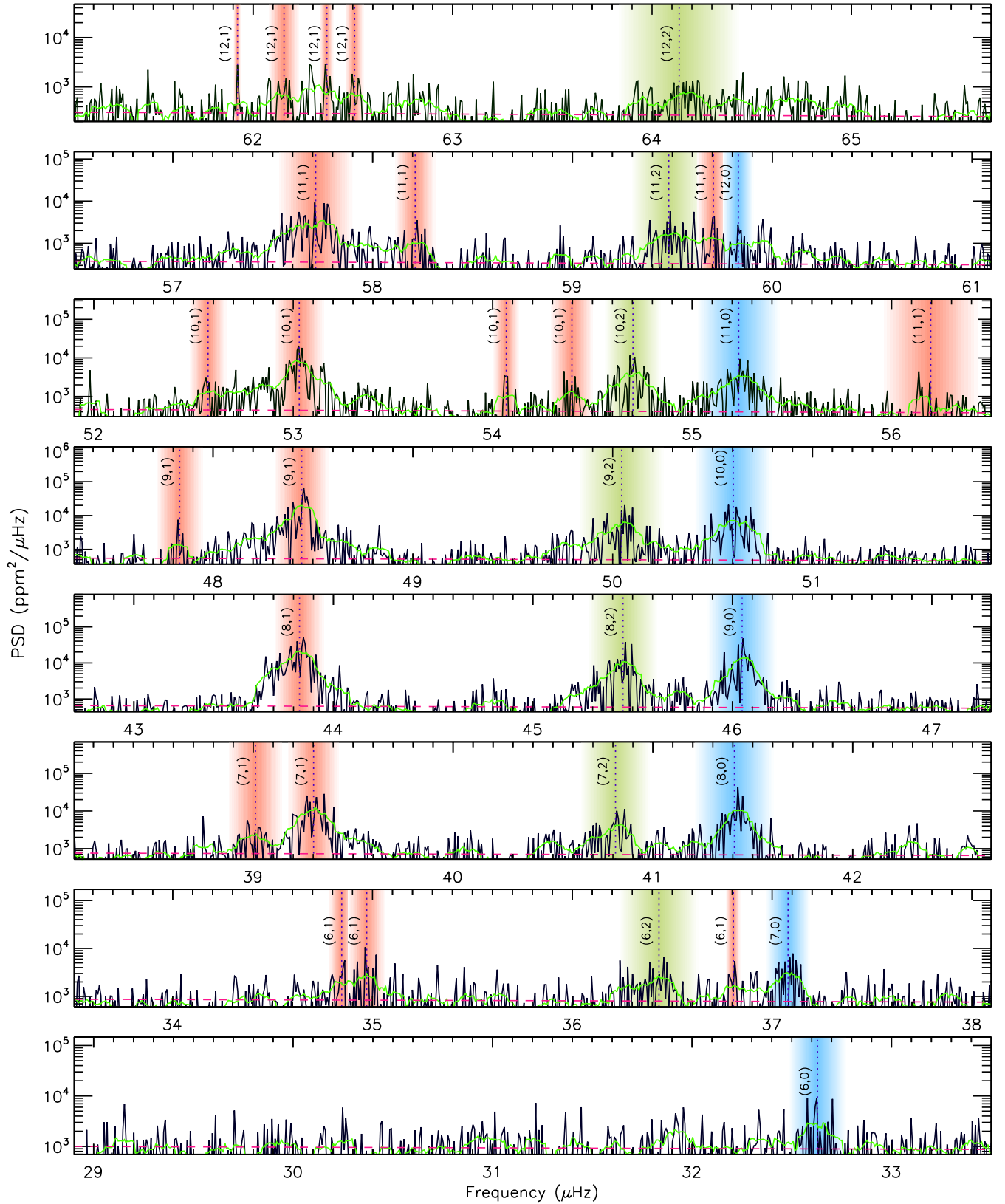


Figure A1. Stacked PSD of KOI-3886 showing the outcome of the peak-bagging process. The green curve is a smoothing of the power density by an amount equivalent to the average radial-mode linewidth found by FAMED. The sloping dashed line represents the local background. Extracted individual mode frequencies are tagged according to their pressure radial order (n_p) and angular degree (ℓ), with color bands indicating their 3σ uncertainties.

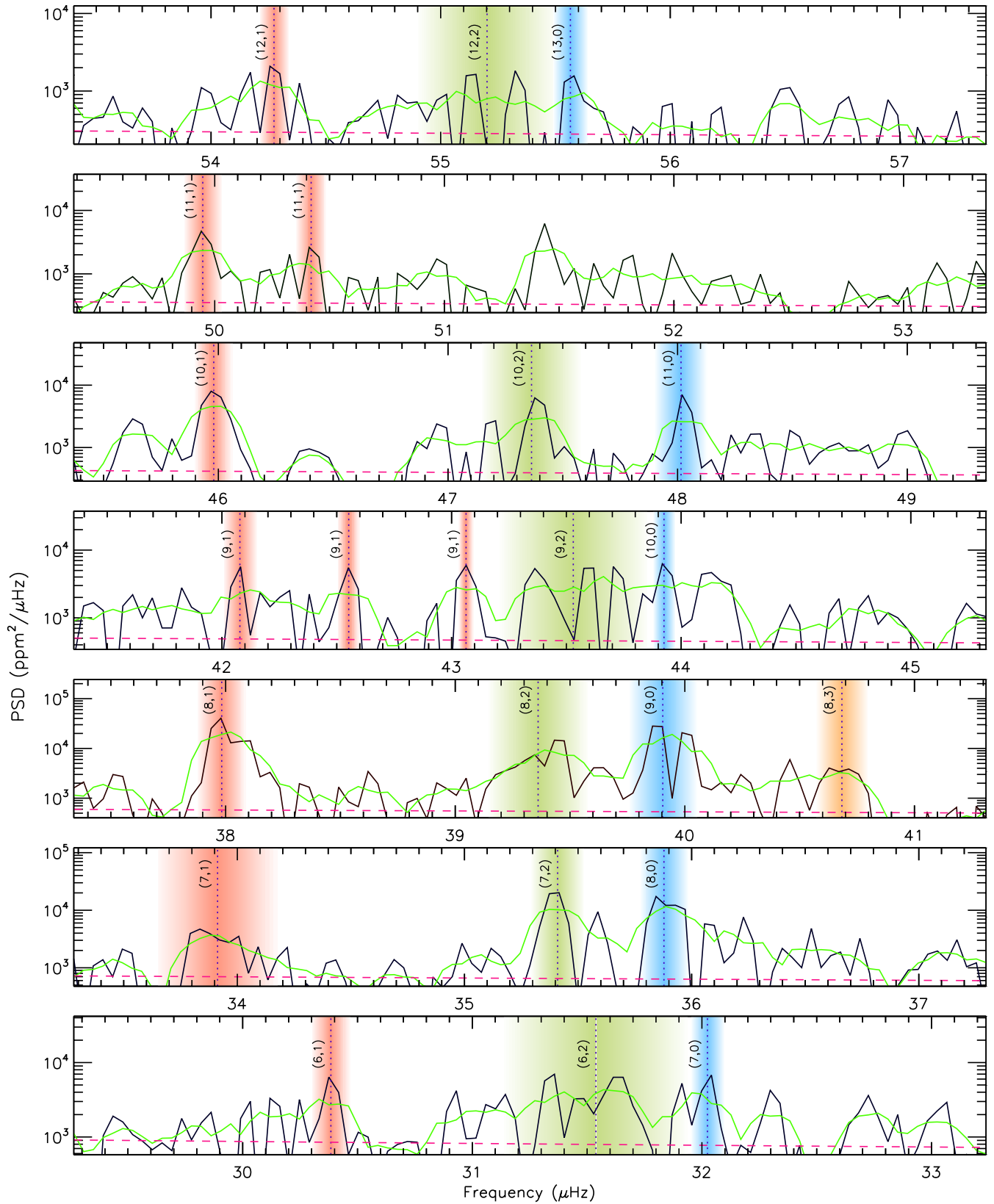


Figure A2. Stacked PSD of ι Dra showing the outcome of the peak-bagging process. Plot style similar to that of Fig. A1. The lower resolution of the TESS power spectrum of ι Dra is readily noticeable.

- 1024 Kane, S. R., Bean, J. L., Campante, T. L., et al. 2021,
 1025 PASP, 133, 014402, doi: [10.1088/1538-3873/abc610](https://doi.org/10.1088/1538-3873/abc610)
- 1026 Khan, S., Hall, O. J., Miglio, A., et al. 2018, ApJ, 859, 156,
 1027 doi: [10.3847/1538-4357/aabf90](https://doi.org/10.3847/1538-4357/aabf90)
- 1028 Kuszlewicz, J. S., Hekker, S., & Bell, K. J. 2020, MNRAS,
 1029 497, 4843, doi: [10.1093/mnras/staa2155](https://doi.org/10.1093/mnras/staa2155)
- 1030 Lagarde, N., Bossini, D., Miglio, A., Vrad, M., & Mosser,
 1031 B. 2016, MNRAS, 457, L59, doi: [10.1093/mnrasl/slv201](https://doi.org/10.1093/mnrasl/slv201)
- 1032 Lenz, P., & Breger, M. 2005, Communications in
 1033 Asteroseismology, 146, 53, doi: [10.1553/cia146s53](https://doi.org/10.1553/cia146s53)
- 1034 Li, T., Bedding, T. R., Christensen-Dalsgaard, J., et al.
 1035 2020, MNRAS, 495, 3431, doi: [10.1093/mnras/staa1350](https://doi.org/10.1093/mnras/staa1350)
- 1036 Li, T., Bedding, T. R., Huber, D., et al. 2018, MNRAS,
 1037 475, 981, doi: [10.1093/mnras/stx3079](https://doi.org/10.1093/mnras/stx3079)
- 1038 Li, T., Li, Y., Bi, S., et al. 2022, arXiv e-prints,
 1039 arXiv:2201.09577. <https://arxiv.org/abs/2201.09577>
- 1040 Lillo-Box, J., Ribas, Á., Montesinos, B., et al. 2021, A&A,
 1041 653, A40, doi: [10.1051/0004-6361/202141158](https://doi.org/10.1051/0004-6361/202141158)
- 1042 Lomb, N. R. 1976, Ap&SS, 39, 447,
 1043 doi: [10.1007/BF00648343](https://doi.org/10.1007/BF00648343)
- 1044 Lundkvist, M. S., Huber, D., Silva Aguirre, V., & Chaplin,
 1045 W. J. 2018, Characterizing Host Stars Using
 1046 Asteroseismology, ed. H. J. Deeg & J. A. Belmonte
 1047 (Springer, Cham), 177,
 1048 doi: [10.1007/978-3-319-55333-7_177](https://doi.org/10.1007/978-3-319-55333-7_177)
- 1049 Magic, Z., Serenelli, A., Weiss, A., & Chaboyer, B. 2010,
 1050 ApJ, 718, 1378, doi: [10.1088/0004-637X/718/2/1378](https://doi.org/10.1088/0004-637X/718/2/1378)
- 1051 Marfil, E., Tabernero, H. M., Montes, D., et al. 2020,
 1052 MNRAS, 492, 5470, doi: [10.1093/mnras/staa058](https://doi.org/10.1093/mnras/staa058)
- 1053 Mathur, S., García, R. A., Régulo, C., et al. 2010, A&A,
 1054 511, A46, doi: [10.1051/0004-6361/200913266](https://doi.org/10.1051/0004-6361/200913266)
- 1055 Miglio, A., Brogaard, K., Stello, D., et al. 2012, MNRAS,
 1056 419, 2077, doi: [10.1111/j.1365-2966.2011.19859.x](https://doi.org/10.1111/j.1365-2966.2011.19859.x)
- 1057 Nielsen, M. B., Ball, W. H., Standing, M. R., et al. 2020,
 1058 A&A, 641, A25, doi: [10.1051/0004-6361/202037461](https://doi.org/10.1051/0004-6361/202037461)
- 1059 Nsamba, B., Campante, T. L., Monteiro, M. J. P. F. G.,
 1060 et al. 2018, MNRAS, 477, 5052,
 1061 doi: [10.1093/mnras/sty948](https://doi.org/10.1093/mnras/sty948)
- 1062 Ong, J. M. J., & Basu, S. 2020, ApJ, 898, 127,
 1063 doi: [10.3847/1538-4357/ab9ffb](https://doi.org/10.3847/1538-4357/ab9ffb)
- 1064 Ong, J. M. J., Basu, S., & McKeever, J. M. 2021a, ApJ,
 1065 906, 54, doi: [10.3847/1538-4357/abc7c1](https://doi.org/10.3847/1538-4357/abc7c1)
- 1066 Ong, J. M. J., Basu, S., & Roxburgh, I. W. 2021b, ApJ,
 1067 920, 8, doi: [10.3847/1538-4357/ac12ca](https://doi.org/10.3847/1538-4357/ac12ca)
- 1068 Paxton, B., Bildsten, L., Dotter, A., et al. 2011, The
 1069 Astrophysical Journal Supplement Series, 192, 3,
 1070 doi: [10.1088/0067-0049/192/1/3](https://doi.org/10.1088/0067-0049/192/1/3)
- 1071 Paxton, B., Cantiello, M., Arras, P., et al. 2013, The
 1072 Astrophysical Journal Supplement Series, 208, 4,
 1073 doi: [10.1088/0067-0049/208/1/4](https://doi.org/10.1088/0067-0049/208/1/4)
- 1074 Paxton, B., Marchant, P., Schwab, J., et al. 2015, The
 1075 Astrophysical Journal Supplement Series, 220, 15,
 1076 doi: [10.1088/0067-0049/220/1/15](https://doi.org/10.1088/0067-0049/220/1/15)
- 1077 Paxton, B., Schwab, J., Bauer, E. B., et al. 2018, The
 1078 Astrophysical Journal Supplement Series, 234, 34,
 1079 doi: [10.3847/1538-4365/aaa5a8](https://doi.org/10.3847/1538-4365/aaa5a8)
- 1080 Pereira, F., Campante, T. L., Cunha, M. S., et al. 2019,
 1081 MNRAS, 489, 5764, doi: [10.1093/mnras/stz2405](https://doi.org/10.1093/mnras/stz2405)
- 1082 Pinçon, C., Takata, M., & Mosser, B. 2019, A&A, 626,
 1083 A125, doi: [10.1051/0004-6361/201935327](https://doi.org/10.1051/0004-6361/201935327)
- 1084 Pires, S., Mathur, S., García, R. A., et al. 2015, A&A, 574,
 1085 A18, doi: [10.1051/0004-6361/201322361](https://doi.org/10.1051/0004-6361/201322361)
- 1086 Reimers, D. 1975, Memoires of the Societe Royale des
 1087 Sciences de Liege, 8, 369
- 1088 Ricker, G. R., Winn, J. N., Vanderspek, R., et al. 2015,
 1089 Journal of Astronomical Telescopes, Instruments, and
 1090 Systems, 1, 014003, doi: [10.1117/1.JATIS.1.1.014003](https://doi.org/10.1117/1.JATIS.1.1.014003)
- 1091 Rogers, F. J., & Nayfonov, A. 2002, ApJ, 576, 1064,
 1092 doi: [10.1086/341894](https://doi.org/10.1086/341894)
- 1093 Rowe, J. F., Coughlin, J. L., Antoci, V., et al. 2015, ApJS,
 1094 217, 16, doi: [10.1088/0067-0049/217/1/16](https://doi.org/10.1088/0067-0049/217/1/16)
- 1095 Roxburgh, I. W. 2016, A&A, 585, A63,
 1096 doi: [10.1051/0004-6361/201526593](https://doi.org/10.1051/0004-6361/201526593)
- 1097 Saunders, N., Grunblatt, S. K., Huber, D., et al. 2022, AJ,
 1098 163, 53, doi: [10.3847/1538-3881/ac38a1](https://doi.org/10.3847/1538-3881/ac38a1)
- 1099 Scargle, J. D. 1982, ApJ, 263, 835, doi: [10.1086/160554](https://doi.org/10.1086/160554)
- 1100 Themeßl, N., Hekker, S., Southworth, J., et al. 2018,
 1101 MNRAS, 478, 4669, doi: [10.1093/mnras/sty1113](https://doi.org/10.1093/mnras/sty1113)
- 1102 Townsend, R. H. D., & Teitler, S. A. 2013, MNRAS, 435,
 1103 3406, doi: [10.1093/mnras/stt1533](https://doi.org/10.1093/mnras/stt1533)
- 1104 Unno, W., Osaki, Y., Ando, H., Saio, H., & Shibahashi, H.
 1105 1989, Nonradial oscillations of stars (Tokyo: University of
 1106 Tokyo Press)
- 1107 Vrad, M., Kallinger, T., Mosser, B., et al. 2018, A&A, 616,
 1108 A94, doi: [10.1051/0004-6361/201732477](https://doi.org/10.1051/0004-6361/201732477)
- 1109 Vrad, M., Mosser, B., & Samadi, R. 2016, A&A, 588, A87,
 1110 doi: [10.1051/0004-6361/201527259](https://doi.org/10.1051/0004-6361/201527259)
- 1111 Zechmeister, M., Reffert, S., Hatzes, A. P., Endl, M., &
 1112 Quirrenbach, A. 2008, A&A, 491, 531,
 1113 doi: [10.1051/0004-6361:200810405](https://doi.org/10.1051/0004-6361:200810405)